

# Theory of shallow and deep boron defects in 4H-SiC

Vitor J. B. Torres,<sup>1</sup> Ivana Capan,<sup>2</sup> and José Coutinho<sup>1,\*</sup>

<sup>1</sup>*13N, Department of Physics, University of Aveiro, Campus Santiago, 3810-193 Aveiro, Portugal*

<sup>2</sup>*Ruđer Bošković Institute, Bijenička 54, 10000 Zagreb, Croatia*

Despite advances toward improving the quality of *p*-type 4H-SiC substrates and layers, we still have no model capable of accounting for the multitude of boron-related optical, junction, and paramagnetic resonance experiments available in the literature. A conspicuous puzzle is the observation of two shallow boron defects with rather distinct axial orientations as found by electron paramagnetic resonance (EPR) and electron nuclear double resonance (ENDOR) data. This feature is not observed in material doped with other group-III elements. Another open issue involves conflicting conclusions from photoluminescence and EPR studies of a deeper boron center, which has been linked to rather distinct models, either based on substitutional or vacancy-related boron defects. We unlock these and other problems by means of first-principles calculations, where the temperature-dependent stability, the electronic activity, and the paramagnetic response of boron defects in 4H-SiC are investigated. [Pre-print published in *Physical Review B* **106**, 224112 (2022)]

DOI:10.1103/PhysRevB.106.224112

Keywords: Point defects; Wide band gap semiconductors; Electron paramagnetic resonance; Density functional calculations

## I. INTRODUCTION

Due to its rugged properties, including mechanical, thermal, and chemical stability, a large breakdown field, and the possibility of growing both electronic-grade *n*- and *p*-type layers, 4H silicon carbide (4H-SiC) is nowadays a semiconductor with an important and growing market on power electronics (used in electric vehicles, power supplies, motor control circuits, and inverters) [1, 2]. SiC also finds applications in fundamental and emerging fields like high-energy particle detection [3] and quantum technologies [4–7].

The *p*-type dopants are usually boron, aluminum, and gallium. As for the former, there is ample evidence that its incorporation leads to the appearance of two types of acceptors, often referred to as *shallow* and *deep* boron centers, owed to the relative depth of their respective levels within the band gap [8, 9]. The two boron species diffuse differently — boron-implanted/diffused layers show heterogeneous incorporation, where the deep center dominates the profile tails [10–12]. While the assignment of the shallow species to substitutional boron on the Si site ( $B_{Si}$ ) seems consensual, the origin of the deep hole trap has remained elusive. Photoluminescence studies favor a boron atom on the carbon site ( $B_C$ ) [13], magnetic resonance experiments point to a boron-vacancy complex [14, 15], whereas first-principles results suggest either  $B_C$  [11, 16] or a boron-silicon-antisite pair [17].

Another problem is that boron is often present in the SiC as a contaminant in trace concentrations. The deep species, also referred to as D-center, is of particular concern, especially in *n*-type SiC where it is negatively charged under equilibrium conditions. This state is a potential trap for holes, threatening the functioning of bipolar devices or *n*-type detectors [18].

A possible route for the elimination of the D-center involves thermal oxidation [19–21]. However, the impact of boron-related minority carrier lifetime degradation is not necessarily

detrimental. The effect was actually explored to improve the switching time characteristics of *p*-*i*-*n* diodes, and that was attributed to the effect of a localized lifetime control in the intrinsic layer due to carrier recombination at deep boron traps [22, 23].

The D-center is known since early deep level transient spectroscopy (DLTS) studies of B doped 6H-SiC, where two nearly overlapping peaks corresponding to electronic transitions at  $E_v + 0.63$  eV and  $E_v + 0.73$  eV were revealed [24]. Suttrop *et al.* [8] found that in addition to the deep boron center (measured in that work as a single DLTS peak at  $E_v + 0.58$  eV), a hole trap at  $E_v + 0.30$  eV was also present, and it was assigned to the shallower boron acceptor.

The presence of the D-center in the 4H polytype was also confirmed using DLTS by Sridhara *et al.* [9]. The level was placed at  $E_v + 0.55$  eV (assuming a  $T^{-2}$ -corrected cross-section), again without resolving a double peak structure. Although the shallower species could not be found by DLTS (the Si/C ratio of the samples did not favor its formation), admittance spectroscopy measurements of Si-poor samples arrived at an acceptor level for shallow boron in the range 284–295 meV above  $E_v$  [9].

Recently, Laplace-DLTS and Laplace-minority carrier transient spectroscopy (Laplace-MCTS) measurements were carried out for studying the shallow and deep boron centers in 4H-SiC [25]. Estimated activation energies for hole emission were respectively 0.27 eV and 0.60 eV. From Laplace-MCTS, it was shown that the D-center consists of two components, D1 and D2 with nearly 1:1 intensity ratio, respectively estimated at  $E_v + 0.49$  eV and  $E_v + 0.57$  eV. The pair of traps was assigned to boron at two different carbon sublattice locations in 4H-SiC. The peak of the shallow boron species was structureless. If it corresponded to the superposition of more than one point defect (in different sublattice sites), they were indistinguishable as far as the resolution offered by Laplace-MCTS.

Early electron paramagnetic resonance (EPR) studies [26] indicated that the symmetry of the shallow boron species in 6H-SiC experienced a remarkable change upon lowering the

\* jose.coutinho@ua.pt

temperature. In the 6H phase, two cubic ( $k_1$  and  $k_2$ ) and one hexagonal ( $h$ ) sites are available for  $B_{Si}$  substitution. While above  $T = 50$  K the EPR signals related to all three substitutions show a trigonal pattern, below that temperature the  $k$ -related signals lower their symmetry to monoclinic. The  $h$ -related signal preserves  $C_{3v}$  symmetry for temperatures as low as 5 K.

These findings were confirmed latter by electron nuclear double resonance (ENDOR) spectroscopy [27, 28]. The defect structure was interpreted as comprising a B-C broken bond, where boron is threefold coordinated (connected to three C ligands), while the remaining C atom holds a hole that is responsible for 40% of the total spin density. Strikingly, whereas the C radical is aligned along the main crystallographic axes for the case of  $B_{Si}$  sitting on the  $h$  site, for some reason, boron on the cubic sites leave a C dangling bond aligned along a basal B-C direction. Analogous observations were reported in 4H-SiC samples [29, 30].

The deep boron center also has EPR-related signals and several experiments produced rich amounts of data (see Refs. 15, 14 and references therein). The defect has a spin-1/2 paramagnetic state, but unlike the shallow boron center, both  $h$ - and  $k$ -related signals show the same alignment along the hexagonal  $c$  axis, with a small basal anisotropy. Minute  $^{13}C$  satellite lines were detected around the main signals, the  $^{11}B$  hyperfine interactions were negligible, and no large  $^{29}Si$  were observed either. However, the spin density was found to be almost 100% localized on Si ligands. Based on the data, a model combining a boron on a silicon position with an adjacent carbon vacancy ( $B_{Si}-V_C$ ) was proposed. The structure comprises an inert boron atom and three Si radicals edging the  $V_C$  unit, thus explaining the electronic and magnetic activity [14, 15]. An obvious difficulty of this model is that for some reason, the pair would have to be invariably formed with an alignment along the  $c$  axis. Such preferential alignment is not supported by first-principles modeling. In fact, the calculations also show that the lowest-lying level of  $B_{Si}-V_C$  is a donor in the upper half of the gap, and therefore, the complex is not compatible with the D-center [16, 17].

While early semi-empirical Hartree-Fock calculations using small H-terminated SiC clusters predicted that  $B_{Si}$  adopts an off-center configuration [31, 32], subsequent supercell calculations within the local density approximation (LDA) to density functional theory (DFT) led to ambiguous conclusions. Accordingly, some authors justified the off-site location of  $B_{Si}$  with a Jahn-Teller (JT) effect [16, 33]. Others found an effective-mass-like defect with no distortion at all [34]. Finally, the authors of Ref. 35 found that the LDA cannot describe the shallow boron state due to overmixing with the valence band. After applying a scissors correction to the band gap during the self-consistent Kohn-Sham method, they obtained a pronounced JT distortion toward  $C_{1h}$ -symmetry and a prominent  $^{13}C$ -hyperfine interaction due to a C-radical [35]. Although they account for the measured localization of the spin density, these results cannot explain the different symmetries of  $k$ - and  $h$ -related boron EPR signals in both 4H- and 6H-SiC.

It is well-known that local and semilocal approximated DFT poorly describes insulator/semiconductor band gaps,

making the discussion of defect properties, in particular those that involve gap states, vulnerable. For instance, several insufficiencies of conventional DFT and advancements in modeling the electronic structure of defects in SiC were presented in Ref. [36]. Among the findings it was shown that hybrid DFT, which replaces a fraction of the local exchange potential by a (possibly screened) Fock exchange contribution, can provide reliable electronic structure of defects in SiC where a local density description fails. We revisited the theory of substitutional boron defects to verify if modern electronic structure calculation methods, in particular hybrid density functional theory, can shed light on the open issues described above. After detailing the methods employed in Sec. II, we report on the physical picture of Si and C replacements by boron in 4H-SiC (Secs. III A and III B). The following three sections connect our findings with photoluminescence and junction capacitance spectroscopies (Sec. III C), with finite-temperature effects on the preferential formation of Si or C substitutions (Sec. III D), as well as with the available EPR/ENDOR measurements (Sec. III E).

We show that  $B_{Si}$  and  $B_C$  defects nicely explain the optical, capacitance and magnetic measurements related to shallow and deep boron centers in 4H-SiC, respectively. Importantly, it is argued that the *shallow* label attributed to  $B_{Si}$  should be interpreted as *shallower* than the deep boron center. In other words, the  $B_{Si}$  center has the characteristics of a localized and deep hole trap and not of an effective mass theory (EMT) dopant. The EMT picture for  $B_{Si}$  has been advocated based on (semi-)local density functional results, but we show that higher level hybrid DFT predicts a strong atomistic relaxation upon hole capture at a  $\sim 0.3$  eV deep trap, making the model compatible with the magnetic resonance observations. We rule out an assignment of deep boron to  $B_{Si}-V_C$  based on the calculated  $g$  tensor elements. Along the paper, we also solve several problems, most notably we explain the observation of different orientations of  $g$  tensor and hyperfine interactions for shallow boron on cubic and hexagonal sites and the distinct temperature-dependence of the  $g$  tensors of both centers.

## II. THEORETICAL METHODS

First-principles calculations were carried out using the density functional Vienna *ab initio* simulation package (VASP) [37–40], employing the projector-augmented wave method, thus avoiding explicit treatment of core states [41]. A basis set of plane-waves with kinetic energy of up to 400 eV was used to describe the Kohn-Sham states. Total energies were evaluated self-consistently, using the hybrid density functional of Heyd-Scuseria-Ernzerhof (HSE06) [42, 43] with a numerical accuracy of  $10^{-7}$  eV. When compared to generalized gradient approximated (GGA) calculations [44] — which underestimate the band gap of SiC by a factor of nearly one half — the HSE06 functional has the main advantage of predicting a Kohn-Sham band gap width of 3.17 eV for 4H-SiC. This figure should be compared to the experimental value of 3.27 eV [45].

Defect energies were found using 400-atom (defect-free) supercells of 4H-SiC (with hexagonal shape), obtained by replication of  $5 \times 5 \times 2$  primitive cells, into which boron defects were inserted. The equilibrium (calculated) lattice parameters of 4H-SiC were  $a = 3.071 \text{ \AA}$  and  $c = 10.052 \text{ \AA}$ . These are close to the experimental values of  $a = 3.079 \text{ \AA}$  and  $c = 10.081 \text{ \AA}$  [46].

Defect structures were firstly optimized within the HSE06 approximation using  $\mathbf{k} = \Gamma$  to sample the Brillouin zone (BZ), until the largest force became lower than  $0.01 \text{ eV/\AA}$ . On a second step, electronic total energies of the obtained structures were found from single-point calculations with the band structure sampled at a  $\Gamma$ -centered  $2 \times 2 \times 2$  mesh of  $\mathbf{k}$ -points (also within HSE06). In line with Gerstmann *et al.* [35], we found that structural optimizations of  $B_{\text{Si}}$  defects within the GGA led to erroneous results due to overmixing of gap states with the valence band top. An analogous effect attributed to the overmixing of a carbon interstitial ( $C_i$ ) level, in this case with the SiC conduction band bottom, was also pointed out by Gouveia and Coutinho [47], and that will be further discussed below.

Electronic transitions of boron defects were calculated by finding the Fermi energy at crossing points of formation energies for different charge states  $q$ . Defect formation energies ( $E_f$ ) were obtained as a function of the chemical potential of the ‘‘sample’’ constituents, according to the usual formalism (see for instance Refs. 48 and 49),

$$E_f(\mu_i, \mu_e; q) = E_{\text{elec}}(q) - \sum_i n_i \mu_i - n_e \mu_e. \quad (1)$$

The first term on the right-hand side of Eq. 1 is given by  $E_{\text{elec}}(q) = \tilde{E}_{\text{elec}}(q) + E_{\text{corr}}(q)$ , and refers to the electronic energy of the periodic calculation  $\tilde{E}_{\text{elec}}$  shifted by  $E_{\text{corr}}$  to remove the effect of the artificial and infinite array of localized charges when the charge state is  $q \neq 0$ . For that we use the method proposed by Freysoldt, Neugebauer, and Van de Walle [50], generalized for anisotropic materials by Kumagai and Oba [51]. The method uses the axial and transverse dielectric constants of 4H-SiC, calculated as  $\epsilon^{\parallel} = 10.65$  and  $\epsilon^{\perp} = 9.88$ , respectively [52]. See Ref. [53] (and also, Refs. [50–52, 54–56]) for convergence tests to the formation energy of boron defects upon varying the boundary conditions. The second and third terms sum up the chemical potentials  $\mu_i$  of the  $n_i$  neutral atomic species and  $n_e = -q$  extra electrons (with respect to the neutral state) that form the problem. The electronic chemical potential is  $\mu_e = E_v + E_F$ , where  $E_v$  and  $E_F$  are the valence band top and Fermi energies, respectively. The former is obtained as the highest occupied state in a bulk supercell, whereas the latter is an independent variable.

Chemical potentials for  $i = \{\text{Si}, \text{C}\}$  were calculated as

$$\mu_i = \mu_i^0 + (1 - f_i) \Delta E_{\text{SiC}}^f, \quad (2)$$

where  $\mu_i^0$  are energies per atom in pure silicon or carbon (diamond phase),  $\Delta E_{\text{SiC}}^f$  is the heat of formation of SiC estimated as  $\Delta E_{\text{SiC}}^f = \mu_{\text{SiC}}^0 - \mu_{\text{Si}}^0 - \mu_{\text{C}}^0 = -0.62 \text{ eV}$ , with  $\mu_{\text{SiC}}^0$  being the

energy per SiC formula unit in a perfect 4H-SiC crystal. This result is close to the enthalpy of formation  $\Delta H_{\text{SiC}}^f = -0.72 \text{ eV}$  measured at standard conditions [57]. Eq. 2 allows for a variation of the chemical potentials in the range  $\mu_i^0 + \Delta E_{\text{SiC}}^f \leq \mu_i \leq \mu_i^0$  subject to  $0 \leq f_i \leq \sum_i f_i = 1$ , with the upper limit representing  $i$ -rich conditions during the material growth. We will calculate the relative energy of different boron defects, all of which possessing a single boron atom. Although being an irrelevant quantity for this purpose, the chemical potential of boron ( $\mu_B$ ) was found from the  $\alpha$ -rhombohedral ground state phase [12 atoms per unit cell with  $R\bar{3}m$  space group (group No. 166)], with equilibrium lattice parameters  $a = 5.029 \text{ \AA}$  and  $\alpha = 58^\circ$  [58].

We also examined the relative stability of boron acceptors on different lattice sites at finite temperatures. The range of temperatures close to those experienced during epitaxial growth are of particular importance. In this case intrinsic conditions apply, and for acceptors with levels in the lower part of the gap the relevant charge state is the negative one. The difference in the Helmholtz free energy of formation between two boron dopants replacing different crystalline species is obtained as,

$$F(B_{\text{Si}}^-) - F(B_{\text{C}}^-) = \Delta F_{\text{elec}} + \Delta F_{\text{vib}} + \mu_{\text{Si}} - \mu_{\text{C}}. \quad (3)$$

In the above,  $\Delta F_{\text{elec}} = F_{\text{elec}}(B_{\text{Si}}^-) - F_{\text{elec}}(B_{\text{C}}^-)$  is the electronic free energy difference between the two defects, where  $F_{\text{elec}}$  is replaced by the stationary solution of the electronic problem,  $E_{\text{elec}}$  (obtained within hybrid density functional theory). This approximation essentially neglects electronic entropy, and it is justified by the depth of the electronic levels and the negligible density of defect states at the Fermi level under intrinsic conditions [59]. The second term on the right-hand side of Eq. 3 accounts for the vibrational free energy difference between the defects, and for each we have,

$$F_{\text{vib}}(T) = k_B T \sum_{i=1}^{3N-3} \ln \left[ 2 \sinh \left( \frac{\hbar \omega_i}{2k_B T} \right) \right]. \quad (4)$$

The summation above runs over  $3N - 3$  vibrational modes of the  $N$ -atom defective supercell, with respective angular frequencies  $\omega_i$ . Symbols  $k_B$  and  $\hbar$  refer to the Boltzmann and reduced Planck constants, respectively. It is noted that Eq. 4 already accounts for zero-point motion. Chemical potentials in Eq. 3 were found from Eq. 2, after adding a vibrational term  $F_{\text{vib}}/N$  to  $\mu_{\text{Si}}^0$  and  $\mu_{\text{C}}^0$ , obtained from respective supercells of silicon and diamond made of  $N = 64$  atoms, and with the temperature set to  $T = 273.15 \text{ K}$ . Analogously, a vibrational free energy term  $2F_{\text{vib}}/N$  was added to  $\mu_{\text{SiC}}^0$ . For further details regarding the calculation of defect free energies, we direct the reader to Refs. 59, 60, 61 and references therein.

The vibrational mode frequencies of 4H-SiC cells containing boron defects were evaluated in  $N = 72$ -atom cells ( $3 \times 3 \times 1$  primitive cells). We considered the participation of all atoms in the dynamical matrix, whose elements were found from the force derivatives with respect to the atomic positions [61].

The  $g$  tensor and hyperfine (HF) interactions of paramagnetic boron defects were calculated using the gauge including projector augmented wave (GIPAW) method [62] as implemented in the QUANTUM ESPRESSO package [63, 64]. The GIPAW method is based on self-consistent density functional perturbation theory, describing the applied magnetic field and spin-orbit couplings as perturbations. The current implementation pertaining the  $g$  tensor calculation is limited to local and semilocal functionals. Hence, for these calculations, the Kohn-Sham states were found within the GGA [44]. We used hexagonal supercells of 256 atoms, a  $\Gamma$ -centered BZ sampling mesh of  $2 \times 2 \times 2$ , and a plane-wave cutoff  $E_{\text{cut}} = 612$  eV (45 Ry). The computation of reciprocal space derivatives to obtain spin currents in linear magnetic response, makes the calculation of  $g$  tensors rather sensitive to  $\mathbf{k}$ -point sampling [65]. Convergence issues can be especially severe for states whose  $g$  values show large deviations from that of the free-electron. For that reason, we also tested a denser  $3 \times 3 \times 3$  grid in the evaluation of  $g$  values for neutral  $B_{\text{Si}}$ .

Due to erroneous geometries obtained for  $B_{\text{Si}}$  defects within GGA, atomistic structures for the GIPAW calculations were found within HSE06-level (using the VASP code). Such combined approach was successfully used in a recent study of defects in  $\text{Ga}_2\text{O}_3$  [66].

As for the HF coupling tensors  $A$ , they describe the interaction between the electron spin of a paramagnetic state with magnetic nuclei at the defect core. For an axial state along an arbitrary principal direction 3, transverse principal values  $A_1 = A_2$  and the HF tensor can be described by isotropic (a) and anisotropic (b) hyperfine constants, which relate to the diagonalized tensor components as  $a = (2A_1 + A_3)/3$  and  $b = (A_3 - A_1)/3$  [27]. The evaluation of the HF tensors rely on the accurate computation of the spin density embedding the nuclei of interest, and for the case of the isotropic term (also known as Fermi contact), it involves the description of the electron density within the core region. Therefore the use of pseudopotentials implies a core reconstruction from the pseudo-wavefunctions [67].

### III. RESULTS

#### A. Boron on the silicon site: shallow boron

We start by looking at the boron impurity on the Si site. In the neutral charge state, the boron atom was clearly displaced from the perfect lattice site after optimizing the energy with respect to the atomistic geometry. Essentially, boron formed three B-C bonds, leaving an unsaturated C radical. The on-site structure was metastable with a small  $\sim 0.1$  eV barrier along the way toward the off-site ground state structure.

4H-SiC has two distinct sublattice sites, namely cubic ( $k$ ) and hexagonal ( $h$ ), and for each, substitutional boron atoms can form two types of C radicals, namely those polarized along the hexagonal axis of the crystal (labeled with ‘a’ and standing for ‘axial’) and those polarized along the basal bond directions (labeled with ‘b’ and standing for ‘basal’). This

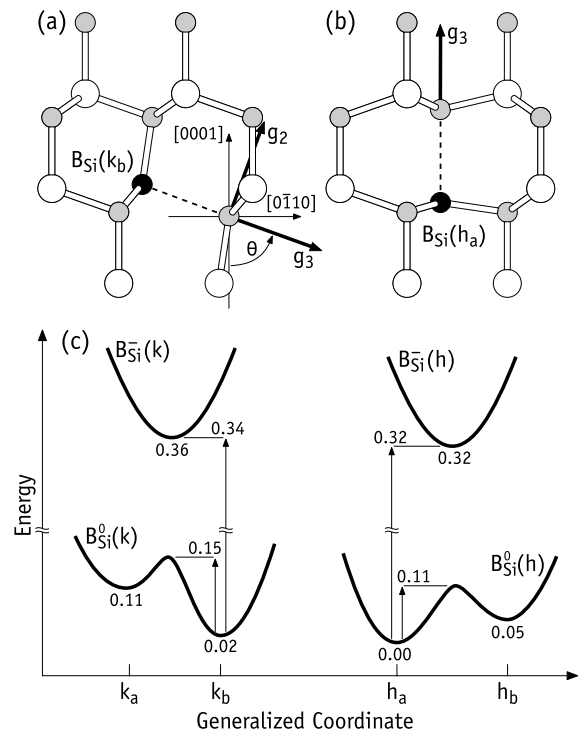


Figure 1. Low energy structures of neutral  $B_{\text{Si}}$  at (a)  $k$  and (b)  $h$  sites of 4H-SiC, respectively, and configurational coordinate diagram of neutral and negatively charge states (c).  $g$  tensor principal directions of neutral states are also shown. Boron, carbon and silicon are shown in black, gray and white, respectively. All energies in the diagram are in eV. Energies located below the energy minima are relative the  $B_{\text{Si}}^0(h_a)$  ground state. Energies next to arrow heads are relative to the state next to the arrow base. See Ref. [53] for details regarding the barrier calculations.

leads to a total of four possible defect configurations to consider.

Among all structures, those depicted in Figs. 1(a) and 1(b), namely  $B_{\text{Si}}(k_b)$  and  $B_{\text{Si}}(h_a)$ , were the most stable at  $k$  and  $h$  sites, respectively. The B atom in both structures displays threefold coordination, where three short (1.65 Å) B-C bonds contrast with the  $\sim 2.42$  Å long separation between B and the C radical (see dashed lines in Fig. 1). See Ref. [53] (and also Ref. [68]), which provides further geometrical details of the structures. While B-C bond lengths are essentially the same for all configurations, the longer B-C distance can vary by about 0.04 Å, depending on the specific site and orientation. The energies of the two most stable neutral states, namely  $B_{\text{Si}}^0(k_b)$  and  $B_{\text{Si}}^0(h_a)$ , differ by 0.02 eV only, whereas  $B_{\text{Si}}^0(k_a)$  and  $B_{\text{Si}}^0(h_b)$  are metastable, respectively at 0.11 eV and 0.05 eV above the ground state  $B_{\text{Si}}^0(h_a)$ . The reason for the breaking of the B-C bond along different directions for  $B_{\text{Si}}(k)$  and  $B_{\text{Si}}(h)$  will become evident when we discuss the electronic structure of the center further below. We summarize the above results in the lower part of the configurational coordinate diagram represented in Fig. 1(c).

The above threefold coordinated  $B_{\text{Si}}$  defects are markedly

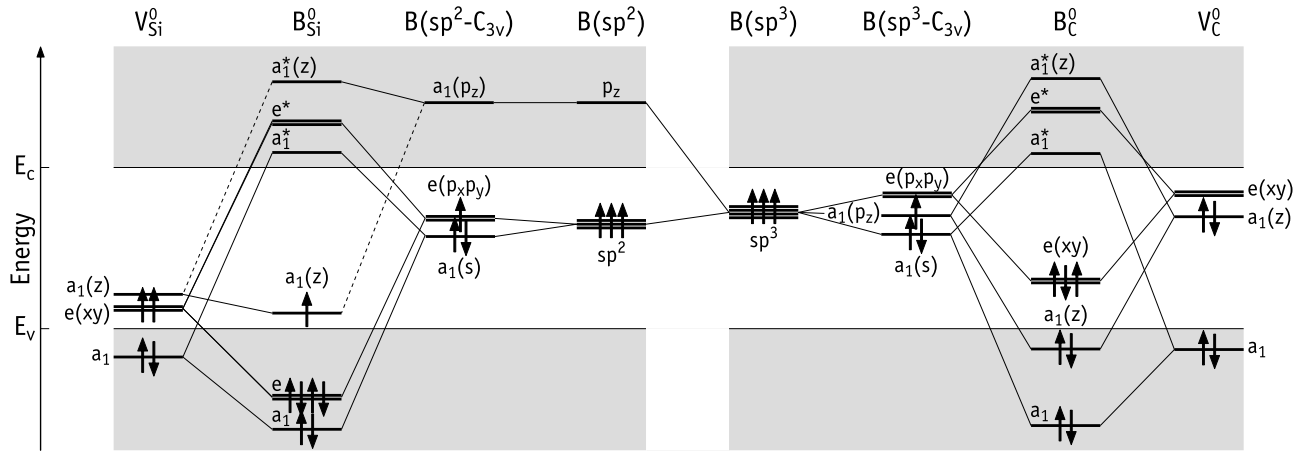


Figure 2. Schematic one-electron models of  $B_{Si}^0$  (left) and  $B_C^0$  (right) impurities in 4H-SiC constructed by hybridization of valence states from  $sp^2$  and  $sp^3$  atomic boron (middle-left and middle-right) with states from the silicon and carbon vacancies (left and right), respectively. Labeling of states is according to the  $C_{3v}$  point group, except for isolated atoms in the middle. Some labels include the direction of the wave function polarization within parentheses. The diagrams are spin-averaged with upward/downward arrows indicating the level occupancy.

different from those found from previous local density functional calculations.  $B_{Si}$  in 3C-SiC was essentially reported as a fourfold coordinated center, showing only slightly different B-C bond lengths due to a weak JT driven  $C_{3v}$  distortion [16, 33]. Four-fold coordination was also found for  $B_{Si}$  in 4H-SiC [34]. The neutral state was in this case interpreted as a shallow acceptor, binding a diffuse hole with the character of an EMT state. These conclusions are clearly at variance with our results — we find that (1) the paramagnetic  $B_{Si}^0$  state is a singlet, showing the highest symmetry allowed by the crystalline host, *i.e.*, it is immune to the JT effect, and (2) is strongly localized on the carbon radical next to boron, which is not in line with an EMT state.

An explanation for the above conflict was put forward by Gerstmann *et al.* [35], who interpreted the prediction of an effective-mass character for  $B_{Si}$  as a failure of LDA, and as a corollary, a failure to describe the measured  $^{13}C$  hyperfine data: “*like the well-known underestimation of the fundamental band gap, the localization of this defect state is also strongly underestimated*”. Accordingly, the LDA gap is about 50% narrower than the measured value, and for that reason, the C dangling bond state becomes artificially over-mixed with the SiC valence states. On the other hand, the non-local HSE06 functional predicts a 3.2 eV wide-gap for 4H-SiC, allowing the singlet acceptor state to emerge above the valence band top.

An analogous effect was found by Gouveia and Coutinho [47] for  $C_i$  in 3C-SiC, but in this case involving the mixing of a gap level with the conduction band. Based on analysis of the Kohn-Sham data of structures ranging between the  $D_{2d}$  (ground state with spin-1) and  $C_{1h}$  (metastable and diamagnetic) structures of  $C_i^0$ , an overestimated mixing between the  $C_i$  highest occupied level and the conduction band states, was attributed to the narrow (semi-)local approximated band gap, which favored the incorrect  $C_{1h}$  structure. Besides the exchange-correlation treatment, this effect may depend on other factors, most notably the dispersion of the defect

state (the mixing could be  $\mathbf{k}$ -point dependent), the sampling of the BZ, or the size/shape of the supercells. The authors of Ref. [47] used 512-atom cubic cells with the Brillouin zone sampled at  $\Gamma$ . More recently, Schultz *et al.* [69] found that upon improving the sampling to  $2 \times 2 \times 2$  (using identical supercells and GGA-level exchange-correlation treatment), the correct spin-1  $D_{2d}$  state could be recovered. In Ref. [36] it was noted that the  $C_{1h}$  metastable structure of  $C_i^0$ , was the most stable when using 216-atom cells with  $\Gamma$ -sampling even at hybrid-DFT level. However, upon adding  $\mathbf{k}$ -points away from  $\Gamma$  to the sampling mesh (where the gap is wider), the correct  $D_{2d}$  configuration was also recovered. The result of Ref. [70], where the  $C_{1h}$  structure was originally proposed as the most stable, was therefore attributed to errors related to calculation settings.

One could ask if, for the case of  $B_{Si}$ , the above effect results from poor sampling of the Brillouin zone. In Ref. [53] we clearly demonstrate that the valence band edge overmixing of  $B_{Si}$  at the GGA-level is a stable result and was found even for high-density  $\mathbf{k}$ -point samplings (up to  $4 \times 4 \times 4$ ).

From inspection of the band structure of defective supercells we arrived at the orbital model for  $B_{Si}^0$  depicted on the left hand side of Fig. 2. It consists of a schematic diagram without spin resolution. Upward/downward arrows simply reflect the electron occupancy. The model postulates how the  $sp^{2\uparrow\uparrow}$  states of atomic B( $sp^2$ ) unfold under the effect of a trigonal crystal field of B( $sp^2-C_{3v}$ ), and how these hybridize with the silicon vacancy states ( $V_{Si}^0$ ) to produce the electronic structure of  $B_{Si}^0$ . Accordingly, three short B-C bonds of  $B_{Si}$  are formed with the participation of six electrons on low-energy bonding states  $a_1 + e$ . These result from overlap of  $a_1$  and  $e(xy)$  states localized on three C atoms edging  $V_{Si}^0$ , with  $a_1(s)$  and  $e(p_x p_y)$  of threefold coordinated B( $sp^2-C_{3v}$ ). Both  $a_1 + e$  and corresponding anti-bonding states  $a_1^* + e^*$  of  $B_{Si}^0$  are resonant with the valence and conduction bands, respectively. The weak interaction between  $a_1(z)$  (localized on the fourth car-

bon radical of  $V_{\text{Si}}^0$ ) with the  $a_1(p_z)$  state from the displaced boron atom, leaves the former within the gap and semioccupied. The  $a_1(z)$  state is the C radical responsible for the acceptor activity of  $B_{\text{Si}}$ , the short covalent B-C bonds naturally explain the off-site distortion without JT effect.

A picture close to that of Fig. 2 was discussed in the literature nearly three decades ago by Bratus and co-workers [31]. From analysis using a linear combination of atomic orbitals (LCAO), it was argued that the  $sp^2 + p_z$  hybridization of boron on the Si site was more stable than  $sp^3$  simply because (1) the covalent radius of B is much smaller than that of Si and (2) the three bonds of  $B(sp^2)$  with carbon ( $\sim 1.6$  Å long) are considerably shorter than the host Si-C bonds ( $\sim 1.9$  Å). Among the main conclusions was also the description of  $B_{\text{Si}}^0$  ground state as a singlet, and consequently, that the observed displacement of B from the perfect crystalline site could be explained without a Jahn-Teller effect.

Subsequent studies of Petrenko *et al.* [32], now using a semi-empirical modified neglect of diatomic overlap method, also supported a pronounced off-site location for  $B_{\text{Si}}$  in SiC. The crystalline host was approximated as a hydrogen saturated spherical cluster of  $\sim 90$  SiC atoms (3C phase). With the emergence of first-principles local density functional supercell calculations, a fourfold coordinated structure for  $B_{\text{Si}}$  with effective-mass character became favored, suggesting that the findings of Ref. [32] resulted from limitations of the method employed. For instance, one could argue that due to quantum confinement and underscreening effects, the band gap of the small clusters was rather wide. That effect could have eliminated the mixing of  $a_1(z)$  with the valence, thus favoring the  $sp^2$ -like bonding of boron. Another argument cautioning against the off-site location of  $B_{\text{Si}}$  is the fact that such relaxations are often overestimated when modeling defects in H-terminated clusters.

On the contrary, we argue that the (semi-)local density functional results for neutral  $B_{\text{Si}}$  are spurious, that hybrid DFT finds the correct off-site location of the B atom, and the LCAO-based arguments of Bratus *et al.* [31] were essentially correct after all. Figure 3 depicts the spin density in the vicinity of neutral  $B_{\text{Si}}(h)$  in 4H-SiC as found for (a) the off-site ground state configuration within hybrid-DFT/HSE06 and (b) the on-site ground state configuration within conventional DFT/GGA. Both isosurfaces have the same spin density cutoff ( $0.003 e/\text{Å}^3$ ). They depict the border within which the magnitude of the spin density is above the specified threshold. Figure 3(a) shows that the amplitude of the spin density near the core of threefold coordinated  $B_{\text{Si}}^0$  is much larger than in the fourfold coordinated configuration. In the latter case, many isosurface *bubbles* (with that specific spin density magnitude) are scattered across the supercell volume, hidden behind the spheres and cylinders used to represent atoms and bonds. Upon decreasing the cutoff by half, no spin density isosurface could be seen for the fourfold coordinated boron, while the p-like state of threefold coordinated boron was well visible. This is consistent with deep threefold and shallow fourfold states, respectively. Clearly, the DFT/GGA approximation predicts a diffuse state with very little localization at the core of the defect.

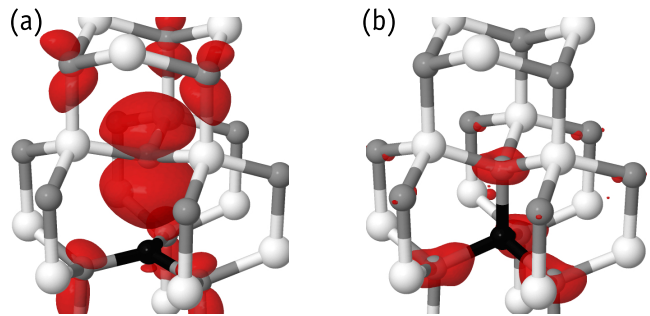


Figure 3. Spin density isosurface (cutoff  $0.003 e/\text{Å}^3$ ) of neutral  $B_{\text{Si}}$  defects at the  $h$  site of 4H-SiC. (a) Off-site threefold coordinated ground state configuration obtained within HSE06. (b) Four-fold coordinated configuration as found from a GGA-level calculation. Si, C and B atoms are shown in white, gray and black, respectively.

Still regarding the bonding character of  $B_{\text{Si}}^0$  in SiC, we note that this center is isovalent to substitutional nitrogen on the Si site of SiC ( $N_{\text{Si}}$ ) [71] as well as substitutional nitrogen in diamond ( $N_{\text{s}}$ ) [72]. Within a simple Lewis picture,  $B_{\text{Si}}^0$  can be represented as  $[\equiv B_{\text{Si}} \bullet C \equiv]$ , where each horizontal bar stands for a single C-B or C-Si bond, and the bullet is an unpaired electron. Analogously,  $N_{\text{Si}}^0$  in SiC and neutral substitutional N in diamond can be described as  $[\equiv N_{\text{Si}} : \bullet C \equiv]$  and  $[\equiv N_{\text{s}} : \bullet C \equiv]$ , respectively, where the dots “:” represent a lone pair of electrons tightly bound to nitrogen and deep within the valence band. Like the B species in the Si site of SiC, N atoms with four carbon nearest neighbors become threefold coordinated next to a paramagnetic C radical. However, unlike  $B_{\text{Si}}$ , local and semilocal density functional calculations account well for their off-site structure [71, 73, 74]. Although an explanation for such behavior is outside the scope of the present work, we speculate that short C-N bonds combined with Coulomb repulsion between the N lone pair and the unpaired electron on the C dangling bond could be important ingredients for the stabilization of the off-site configuration. A strong indication in favor of this argument is that while the C-radical of  $B_{\text{Si}}^0$  in SiC induces a semioccupied state low in the gap, C-radicals of  $N_{\text{Si}}$  in SiC and  $N_{\text{s}}$  in diamond lead to semioccupied states in the upper half of the gap, suggesting a stronger repulsion of the unpaired electron in the N-related defects.

The semioccupied  $a_1^\uparrow(z)$  singlet of  $B_{\text{Si}}^0$  in 4H-SiC is represented in Fig. 2 just above the valence band top. A spin-averaged calculation of  $B_{\text{Si}}^0(h_a)$  reveals that this level is located 0.52 eV above the highest occupied Kohn-Sham level from the bulk. On the other hand, in a spin-polarized calculation the spin-up  $a_1^\uparrow(z)$  level lies within the valence band (the highest occupied state is bulk-like), while the spin-down component of  $a_1(z)$  is 1.47 eV above the  $E_v$  level. This picture is indicative of deep acceptor activity.

Upon atomic relaxation of negatively charged defects ( $B_{\text{Si}}^-$ ), we found that independently of the lattice site and initial configuration, the boron atom moved to the perfect substitutional site, thus forming four nearly equivalent 1.77 Å long B-C

bonds. Concurrently, the  $a_1(p_z)$  state of boron increased its mixing with  $a_1(z)$  from  $V_{\text{Si}}$  to form the fourth B-C bond. The resulting  $a_1(z)$  bond state from  $\text{B}_{\text{Si}}^-$  became resonant with the valence, and the Kohn-Sham band gap was left clean. This does not imply that  $\text{B}_{\text{Si}}^-$  cannot capture a hole to become neutral. It does not imply that it is a shallow acceptor either. As will be shown in Sec. III C, hole capture is accompanied by reconfiguration to the threefold coordinated structure, making the hole trap relatively deep. As summarized in Fig. 1(c), the energy of  $\text{B}_{\text{Si}}^-(h)$  was found slightly lower (0.04 eV) than that of  $\text{B}_{\text{Si}}^-(k)$ .

Now we look at the origin of the site-dependent alignment of  $\text{B}_{\text{Si}}^0$  in 4H-SiC (the arguments discussed below apply to other polytypes as well). The analysis is best followed with help of Fig. 4. In 4H-SiC, the stacking of SiC dimers along the  $c$  axis occurs according to a A-B-C-B sequence, where A and C are hexagonal bilayers and B are cubic bilayers. Importantly, while hexagonal SiC dimers (type A and C) are replicated in steps of length  $c$  along the main crystallographic direction (where  $c$  is the axial lattice parameter), cubic bilayers (type B) are repeated every  $c/2$ -long steps. This results in a wavier electrostatic potential and a stronger electric field in crystalline regions along type B columns (see Fig. 4).

The  $a_1^\uparrow(z)$  state on the C radical of  $\text{B}_{\text{Si}}^0(k_a)$  interacts with the extensive  $3sp^3$  valence electrons of the nearest Si atom along the axis, only  $c/2 - r_0 = 3.14 \text{ \AA}$  away from carbon, where  $r_0$  is the Si-C bond length (see left hand side of Fig. 4). This repulsion effectively raises the energy of  $\text{B}_{\text{Si}}^0(k_a)$  by 0.11 eV with respect to  $\text{B}_{\text{Si}}^0(h_a)$ . In the latter case, the Si atom on the back of the  $\text{C} \cdots \text{B}_{\text{Si}}(h_a)$  unit is  $c - r_0 = 8.17 \text{ \AA}$  away from C (see right hand side of Fig. 4).

Due to symmetry reasons, the above analysis cannot be strictly applied to  $\text{B}_{\text{Si}}^0(k_b)$  and  $\text{B}_{\text{Si}}^0(h_b)$  defects (with C radicals polarized along Si-C basal bonds). However, analogous conclusions may be drawn by inspecting the amount of empty space between the carbon radical and the nearest atom along the  $\text{B} \cdots \text{C}$  direction. As depicted in the middle of Fig. 4, in a pristine 4H-SiC crystal, that distance is  $3c/4 - r_0 = 5.64 \text{ \AA}$  for both  $k$  and  $h$  sites, thus lying right between the lower and upper limits of the axially distorted configurations. This is consistent with the energy ordering found for  $\text{B}_{\text{Si}}^0(h_a) < \text{B}_{\text{Si}}^0(k_b) \sim \text{B}_{\text{Si}}^0(h_b) < \text{B}_{\text{Si}}^0(k_a)$ .

The reorientation barrier between basal and axial distortions of neutral  $\text{B}_{\text{Si}}$  defects, was found from a batch of nudged elastic band (NEB) calculations encompassing five intermediate structures between initial and final states. See Ref. [53] (and also Ref. [75]) for details of the barrier calculations. From the results we find activation barriers of 0.04 eV and 0.06 eV for  $k_a \rightarrow k_b$  and  $h_b \rightarrow h_a$  reorientations. These jumps involve a return from metastable to lowest energy structures of  $\text{B}_{\text{Si}}^0$  in  $k$  and  $h$  sites, respectively. These figures are reflected in the diagram of Fig. 1(c). Given the above meV-range barriers, the metastable states are probably not formed, even at liquid-He temperature.

The reorientation of the C radical of  $\text{B}_{\text{Si}}(k)$  between equivalent basal orientations was also investigated using the NEB

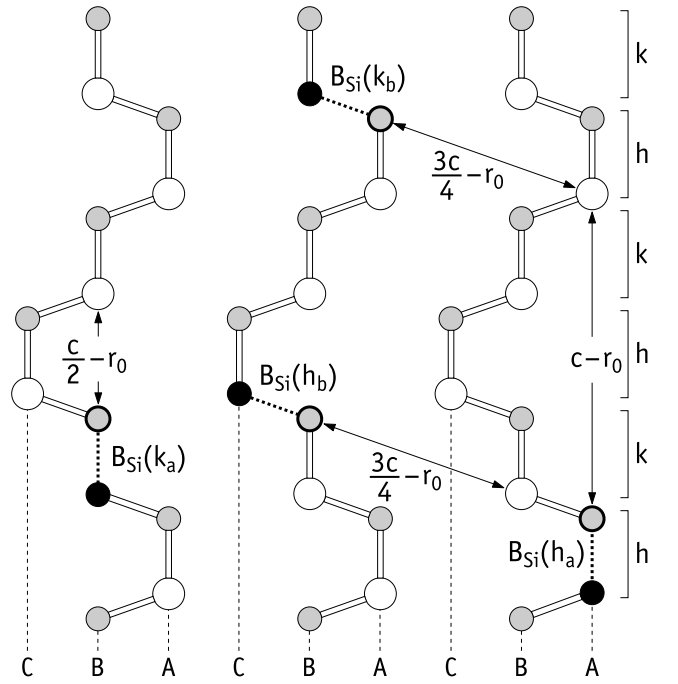


Figure 4. Location and possible alignments of  $\text{B}_{\text{Si}}$  defects on the  $\{11\bar{2}0\}$  plane of 4H-SiC. Silicon and carbon atoms are shown in white and gray. Boron and carbon at the core of the defect are represented as black and gray-haloed circles. For the sake of clarity, all atomic positions are those of the perfect crystal. The C-B broken bond of the neutral state is represented as a dotted line. Relevant distances are indicated next to arrows, where  $c$  and  $r_0$  are the axial lattice parameter and the Si-C bond length, respectively. Stacking (A, B, C) and site ( $k$ ,  $h$ ) indexes are also indicated.

method. We found that  $\text{B}_{\text{Si}}(k)$  has to surmount a barrier of 0.09 eV to perform a  $k_b \rightarrow k_b'$  jump between neighboring alignments with the same energy. Hence, above a certain (low) temperature,  $\text{B}_{\text{Si}}(k)$  is likely to roam around all equivalent  $k_b$  distortions, showing effective thermally averaged  $C_{3v}$  symmetry.

## B. Boron on the carbon site: deep boron

Regarding the boron replacement of carbon ( $\text{B}_{\text{C}}$ ), we found that the boron impurity sits very close to the crystalline site. Very small B-C bond distortions were obtained when symmetry breaking was allowed during the relaxations. From inspection of the Kohn-Sham band structure we found that the on-site configuration (with  $C_{3v}$  symmetry) introduces a deep doublet state in the gap. In a spin-averaged calculation of a trigonal  $\text{B}_{\text{C}}^0(h)$  defect, a pair of doubly degenerate Kohn-Sham states occupied by three electrons appear at 0.29 eV above the highest occupied level from the bulk. On the other hand, in a spin-polarized calculation of the same structure the spin-up  $e^{\uparrow}(xy)$  level lies at 0.06 eV above  $E_v$ , whereas the spin-down counterpart  $e^{\downarrow}(xy)$  is 0.44 eV above the  $E_v$ . Note that these figures neglect any Jahn-Teller relaxation and electron-

phonon coupling effects (the occupation of the doublets was fixed — not variational).

A simplified bond orbital model for neutral  $B_C$  is shown on the right half of Fig. 2. It represents the conversion of atomic boron  $B(sp^3)$  states under the effect of a trigonal crystal field,  $B(sp^3-C_{3v})$ , and the hybridization of the later with  $a_1^\uparrow + a_1^\downarrow(z) + e(xy)$  states of the carbon vacancy (where boron is sitting). The Si radicals edging the  $V_C$  defect are considerably more diffuse than the C radicals in  $V_{Si}$ , and therefore their overlap with boron is significant for all states. The result is the formation of bonding  $a_1^\uparrow + a_1^\downarrow(z)$  and anti-bonding  $a_1^* + a_1^*(z)$  singlets within the valence and conduction bands, respectively, while a partially occupied  $e^{\uparrow\downarrow}(xy)$  doublet is left in the gap. The  $a_1$  and  $a_1(z)$  states are respectively located on basal and axial B-Si bonds, while the components of  $e(xy)$  are B-centered  $p_x$ - and  $p_y$ -like states overlapping basal bonds only. It is clear that any electronic activity of  $B_C$  must be ascribed to the  $e(xy)$  state.

Upon monoclinic distortion ( $C_{1h}$  symmetry), the  $e^{\uparrow\downarrow}(xy)$  neutral state can either split into  $a''^{\uparrow\downarrow}(x) + a'^{\uparrow}(y)$  or  $a'^{\uparrow\downarrow}(y) + a''^{\uparrow}(x)$  states with net spin  $S = 1/2$ . Here  $a'$  and  $a''$  are respectively symmetric and anti-symmetric with respect to a  $\{2\bar{1}\bar{1}0\}$  mirror plane. While  $a''$  is a  $p_x$ -like state with a node coincident with the mirror plane,  $a'$  is  $p_y$ -like with a node on the boron atom and polarized along  $\langle 01\bar{1}0 \rangle$ . Irrespectively of the lattice site, we found that the most stable JT-distorted configuration of  $B_C^0$  involved a minute ( $\sim 0.06$  Å) displacement of boron along  $\langle 01\bar{1}0 \rangle$ , leading to two shorter B-Si bonds (and a slightly elongated one). That configuration corresponds to the electronic state  $a'^{\uparrow\downarrow} + a''^{\uparrow}$ . The alternative  $a''^{\uparrow\downarrow} + a'^{\uparrow}$  state was metastable by 15 meV only. In overall,  $B_C^0(k)$  was more stable than  $B_C^0(h)$  by 39 meV.

Interestingly, and despite the minute JT-driven bond deformations, the relaxation energy with respect to the high-symmetry ( $C_{3v}$ ) state was about 0.25 eV for both  $B_C^0(k)$  and  $B_C^0(h)$ . This is a surprisingly large value, and as far as we could find, it is not an artifact. The electronic occupancy of the high symmetry state (at the JT singularity) was not variational during the self-consistent cycle, and each pair of spin components of the doublet kept equal occupancy.

While the JT relaxation energy is a considerable barrier to surmount at liquid-He temperature, the question is — how likely is boron able to jump between neighboring off-axis configurations and show a dynamic Jahn-Teller effect? There are in total 6 possible JT displacements of boron away from the perfect C-site. They comprise alternating  $a'^{\uparrow\downarrow} + a''^{\uparrow}$  and  $a''^{\uparrow\downarrow} + a'^{\uparrow}$  states around the hexagonal axis of the crystal, dephased by a rotation angle of  $\pi/3$ . Jumping between neighboring structures involves a displacement of the B atom of only 0.04 Å. Although the barrier was not calculated with a proper transition-state method, it was estimated from the energy of the structure at mid-way between two neighboring  $B_C^0(k)$  and  $B_C^0(h)$  states. The small traveling distance of the B atom justifies this simple approach. Accordingly, we found that the rotation barrier is about 15 meV for both  $B_C^0(k)$  and  $B_C^0(h)$ . Such minute figure is smaller than the zero-point energy of an oscillating B-Si bond, suggesting that the  $B_C^0$  defects ef-

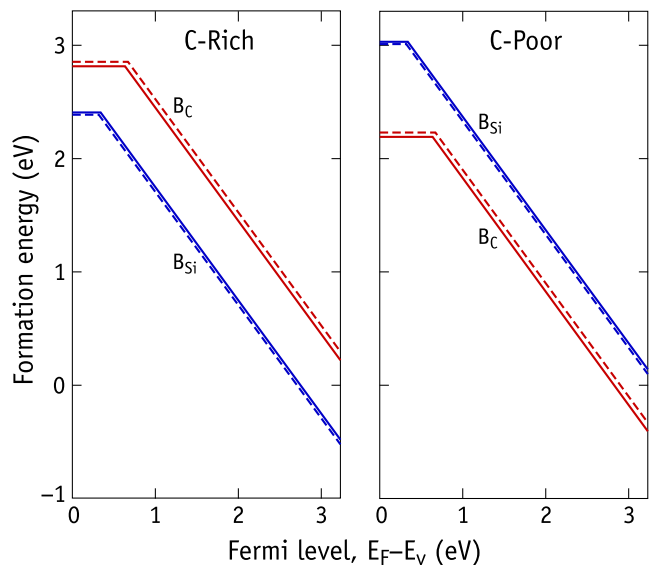


Figure 5. Formation energy diagrams of  $B_{Si}$  (blue lines) and  $B_C$  (red lines) in 4H-SiC. Solid and dashed lines represent formation energies of boron defects located at  $k$  and  $h$  sites, respectively.

fectively roam around the  $c$  axis, thus showing a dynamic-JT effect even at liquid-helium temperature.

In the negative charge state, the doublet becomes fully occupied and  $B_C^-$  recovers the full trigonal symmetry of the C-site. In this charge state, the impurity at the  $k$ -site is 76 meV more stable than at the  $h$ -site.

### C. Connection with optical and junction spectroscopy

The formation energy of boron impurities, obtained according to Eq. 1, is shown in Fig. 5. There we show the results for the formation energy of  $B_{Si}$  and  $B_C$  defects in 4H-SiC under carbon rich and poor conditions (left- and right-hand side diagrams, respectively), as a function of the Fermi energy (referred with respect to the valence band top). Solid and dashed lines refer to boron defects located at  $k$  and  $h$  sites, respectively.

Clearly, and in agreement with previous findings [16, 33], in carbon rich material, where depletion of Si is favored,  $B_{Si}$  has lower formation energy than  $B_C$ . The opposite is found for C-poor material. At growth temperatures, where the Fermi level can be assumed to be at mid-gap, the formation energy of  $B_{Si}$  is 0.74-0.85 eV lower than that of  $B_C$  in C-rich samples. On the other hand,  $B_C$  is more stable than  $B_{Si}$  by 0.36-0.48 eV in C-poor samples. The ranges result from considering  $k$  and  $h$  sites for each impurity.

Figure 5 shows that both  $B_{Si}$  and  $B_C$  are single acceptors. The defects adopt a negative charge state for a wide range of Fermi levels, and we did not find donor transitions or additional acceptor transitions within the gap.

Considering the lowest-energy configurations of neutral  $B_{Si}$  defects at  $k$  and  $h$  sites, we place the acceptor levels of  $B_{Si}(k)$



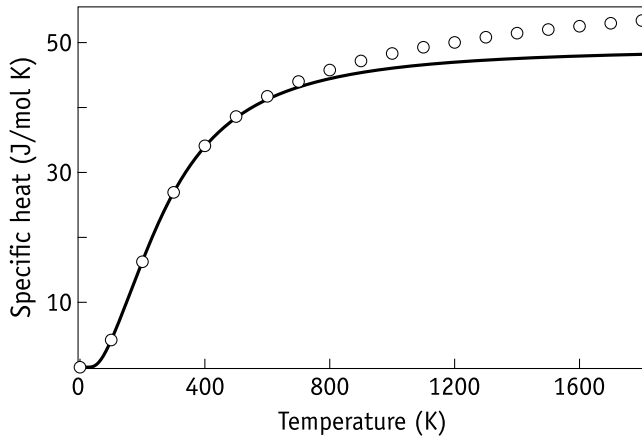


Figure 6. Specific heat of 4H-SiC calculated at constant volume within the harmonic approximation (solid line). Circles represent measured data for  $\alpha$ -SiC, obtained under constant pressure conditions as reported in Ref. [76]. The calculation employed Eq. 5 and considered a total of 213 vibrational frequencies from a 72-atom 4H-SiC supercell.

and  $B_{Si}(h)$  at  $E_v + 0.34$  eV and  $E_v + 0.32$  eV, respectively. These results are shown graphically in Fig. 1(c), and they indicate that the binding energy of the hole to  $B_{Si}$  is almost independent of the lattice site, despite the adoption of rather distinct crystalline alignments by neutral  $B_{Si}(k_b)$  and  $B_{Si}(h_a)$  ground states.

These results are in line with the observation of a single peak by DLTS and Laplace-DLTS related to a hole trap of shallow boron at  $E_v + 0.27$  eV [8, 18, 25]. Despite the agreement, we note that the calculated difference between the acceptor levels of  $B_{Si}$  at  $k$  and  $h$  site (20 meV), is smaller than the typical error of the method employed for the calculation. Additionally, the detection of a single peak by the Laplace-DLTS technique suggests that the difference could be even smaller, or that one of the configurations is dominant. The calculated relative energies of  $B_{Si}(k)$  and  $B_{Si}(h)$  do not support the second possibility.

An important question relates to the mechanism behind the capture of holes by  $B_{Si}^-$ . After all, the band structure of a supercell with this defect state shows a clean band gap. Our findings indicate that the mechanism involves a strong electron-phonon coupling, much like in a polaronic trapping effect [77]. Essentially, the off-site distortion of  $B_{Si}^-$  raises an occupied level above the valence band top, which is then stabilized upon hole capture. The first stage (level raising above  $E_v$ ) translates into the surmounting of a capture barrier, estimated to be of the order of 0.1 eV. See Ref. [53] (and also Refs. [78–82]) for details regarding the raising of the level above  $E_v$  and the estimation of the capture barrier.

Regarding boron on the carbon site, we find  $(-/0)$  transitions at  $E_v + 0.63$  eV and  $E_v + 0.67$  eV for  $B_C(k)$  and  $B_C(h)$ , respectively. Neutral ground states with electronic configuration  $a'\uparrow\downarrow + a''\uparrow$  were considered in our calculations. These figures agree well with early and recent measurements in 6H-

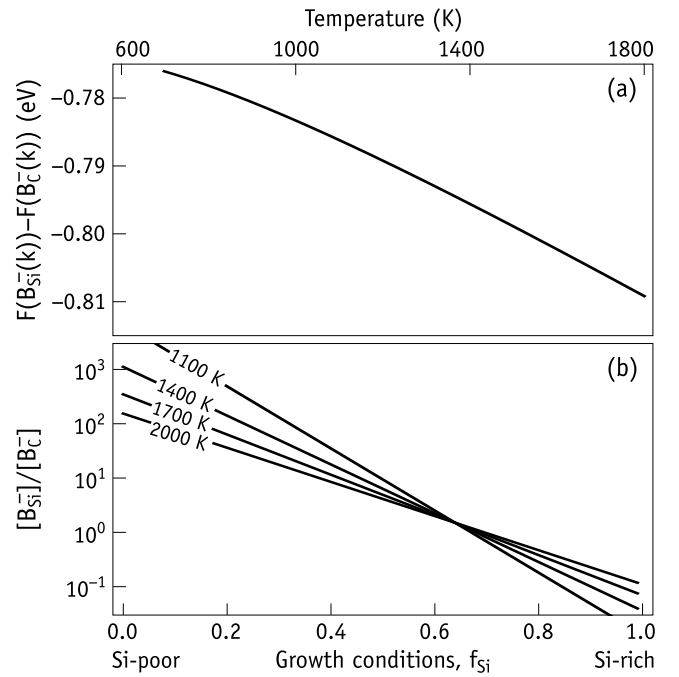


Figure 7. (a) Free energy of  $B_{Si}^-(k)$  with respect to that of  $B_C^-(k)$  in 4H-SiC as a function of temperature under Si-poor conditions. The Fermi level was considered to be located at midgap. (b) Concentration ratio of  $B_{Si}^-$  to that of  $B_C^-$  as a function of the stoichiometric growth conditions (represented by  $f_{Si}$ ), for selected temperatures.

and 4H-SiC [8, 9, 18, 24, 25], which indicate a transition of deep boron in the range 0.5-0.7 eV above the valence band top.

The separation between calculated levels of  $B_C(k)$  and  $B_C(h)$  is small,  $\approx 40$  meV, but about twice larger than the analogous figure obtained for  $B_{Si}$ . Again, this difference is lower than the error of the calculations, and therefore should be considered with due care. Considering that the signal of the D center was recently shown to comprise two equally intense peaks separated by nearly 0.1 eV, our results support the view that these peaks arise from two nearly equivalent deep boron acceptors: a “shallower” configuration sitting at the cubic carbon site and a “deeper” one replacing the hexagonal site. These correspond to measured transitions at  $E_v + 0.49$  eV and  $E_v + 0.57$  eV, respectively [25].

#### D. Finite temperature calculations

Up until now, our results refer to zero temperature conditions, not even accounting for differences in zero-point motion between  $B_{Si}$  and  $B_C$  species. However, at high temperatures the effect of entropy to the relative stability of  $B_{Si}$  and  $B_C$  can be relevant. To strengthen our conclusions, we evaluated their respective free energies of formation at high temperatures, in particular under intrinsic conditions. For the sake of testing the methodology we calculated the specific heat at constant volume for bulk 4H-SiC as,

$$c_v(T) = -T \left( \frac{\partial^2 F_{\text{vib}}}{\partial T^2} \right), \quad (5)$$

and the result is shown in Fig. 6. In that plot, we also report several data points recorded during experiments at constant pressure for  $\alpha$ -SiC (6H-SiC) [76].

The calculated specific heat describes the measurements very well up to nearly  $T \sim 800$  K, when anharmonic effects start to gain importance, and beyond which the calculated free energy and its derivatives become more qualitative. In Ref. [61], we demonstrated that these calculations cannot be improved by enlarging the supercells. Also important, is the fact that the constant volume calculations match well the constant pressure measurements across a wide range of temperatures. The reason is hinted by the minute thermal expansion of crystalline SiC, which is about  $5 \times 10^{-6} \text{ K}^{-1}$  for temperatures as high as  $1000^\circ \text{C}$  [46].

The calculated difference in the free energy of formation  $\Delta F(k) = F(\text{B}_{\text{Si}}^-(k)) - F(\text{B}_{\text{C}}^-(k))$ , is shown in Fig. 7(a) in the temperature range  $T = 600\text{-}1800$  K. The quantity represented refers to impurities located in cubic sites. For boron defects at the hexagonal sites the  $T$ -dependence of the analogous quantity was almost identical, although its magnitude increased by about 0.1 eV. Figure 7(a) shows that  $\text{B}_{\text{Si}}^-$  increases its relative stability with respect to  $\text{B}_{\text{C}}^-$  by almost 0.05 eV when raising the temperature from 1000 K to 2000 K. The implication of this result is illustrated in Fig. 7(b) where we plot the concentration ratio of  $\text{B}_{\text{Si}}^-$  to  $\text{B}_{\text{C}}^-$  defects as a function of the stoichiometric conditions (represented by  $f_{\text{Si}}$ ), at different temperatures. Under equilibrium, the concentration ratio is given by

$$\frac{[\text{B}_{\text{Si}}^-]}{[\text{B}_{\text{C}}^-]} = \exp \left( - \frac{\Delta F(k) - \Delta F(h)}{k_{\text{B}}T} \right), \quad (6)$$

where  $\Delta F(k)$  and  $\Delta F(h)$  are free energy differences  $F(\text{B}_{\text{Si}}^-) - F(\text{B}_{\text{C}}^-)$  pertaining  $k$  and  $h$  sites, respectively [as represented in Fig. 7(a)]. For chemical vapor deposition grown material, reactors typically run at temperatures of about  $1600\text{-}1650^\circ \text{C}$  ( $T \sim 1900$  K) [83]. Under these conditions we estimate  $[\text{B}_{\text{Si}}^-]/[\text{B}_{\text{C}}^-] \approx 200$  and about 0.1 for a Si-poor and Si-rich stoichiometry, respectively. It is evident that even for the limit of Si-poor growth, which is the most favorable for introduction of the  $\text{B}_{\text{Si}}$ , thermodynamics imposes the formation of deep boron centers with a concentration about two orders of magnitude below that of the shallow counterpart. Figure 7(b) shows that even at  $T = 1700$  K the  $[\text{B}_{\text{Si}}^-]/[\text{B}_{\text{C}}^-]$  ratio is nearly 350, and probably the elimination of  $\text{B}_{\text{C}}$  cannot be achieved during growth.

We finally note that from the calculated vibrational mode frequencies, we could not find boron-related modes outside the spectrum of the crystalline density of states. Therefore any boron vibrational mode must be resonant, and most certainly hard to detect experimentally.

Table I. Calculated principal values ( $g_1$ ,  $g_2$  and  $g_3$ ) of the gyromagnetic  $g$  tensor of paramagnetic boron-related defects at  $k$  and  $h$  sites of 4H-SiC. Assignments of experimental values from EPR signals of shallow (top) and deep (bottom) boron centers are indicated by their location in the table. For trigonal states ( $C_{3v}$ ),  $g_3$  is parallel to the main crystallographic  $c$  axis. For monoclinic states ( $C_{1h}$ ),  $g_1$  is perpendicular to the  $\{2\bar{1}\bar{1}0\}$  symmetry plane, while  $g_2$  and  $g_3$  are rotated by an angle  $\theta$  away from  $\langle 0\bar{1}10 \rangle$  and  $\langle 0001 \rangle$  directions, respectively. Dynamic trigonal states (labeled with a subscripted “dyn”) refer to averaged  $g$  tensors involving three symmetrically equivalent  $C_{1h}$  states (see text). Also indicated are the temperatures of the measurements.

	$T$ (K)	Sym	$g_1$	$g_2$	$g_3$	$\theta$ ( $^\circ$ )
$\text{B}_{\text{Si}}^0(k_b)$		$C_{1h}$	2.0068	2.0078	2.0028	70
EPR [29]	4.2-45	$C_{1h}$	2.0059	2.0069	2.0025	69
$\text{B}_{\text{Si}}^0(k_{\text{dyn}})$		$C_{3v}$	2.0051	2.0051	2.0073	0
EPR [29]	61-83	$C_{3v}$	2.0046	2.0046	2.0064	0
$\text{B}_{\text{Si}}^0(h_a)$		$C_{3v}$	2.0089	2.0089	2.0022	0
EPR [29]	4.2-83	$C_{3v}$	2.0070	2.0070	2.0019	0
$\text{B}_{\text{Si}}(k)\text{-V}_{\text{C}}^0(k)$		$C_{1h}$	2.0041	2.0065	2.0028	78
$\text{B}_{\text{Si}}(k)\text{-V}_{\text{C}}^0(k_{\text{dyn}})$		$C_{3v}$	2.0035	2.0035	2.0063	0
$\text{B}_{\text{C}}^0(k)$		$C_{1h}$	2.0050	2.0205	2.0279	13
$\text{B}_{\text{C}}^0(k_{\text{dyn}})$		$C_{3v}$	2.0129	2.0129	2.0275	0
EPR [14]	4	$\sim C_{3v}$	2.0	2.0	2.029	$\sim 0$
$\text{B}_{\text{C}}^0(h)$		$C_{1h}$	2.0056	2.0173	2.0246	13
$\text{B}_{\text{C}}^0(h_{\text{dyn}})$		$C_{3v}$	2.0116	2.0116	2.0240	0
EPR [14]	4	$\sim C_{3v}$	2.0	2.0	2.024	$\sim 0$

### E. Connection with EPR

Figure 1 readily explains the rather distinct EPR signals of shallow boron at  $k$  and  $h$  sites, as well as their temperature dependence [26]. While  $\text{B}_{\text{Si}}^0(h)$  finds its ground state forming a paramagnetic p-like orbital on the C atom of a broken B-C bond along the main crystalline axis, the  $\text{B}_{\text{Si}}^0(k)$  lowest energy configuration has an analogous p-orbital (and a B-C broken bond) but it is now along the direction of a basal bond of the crystal.

The upper part of Tab. I records the calculated  $g$  tensors of shallow  $\text{B}_{\text{Si}}^0$  defects in 4H-SiC, along with the corresponding quantities measured by EPR [29]. For trigonal states ( $C_{3v}$  symmetry), the main  $g_3$  component is assumed to be parallel to the main crystallographic  $c$  axis. For monoclinic states ( $C_{1h}$  symmetry),  $g_1$  is perpendicular to the  $\{2\bar{1}\bar{1}0\}$  symmetry plane, while  $g_2$  and  $g_3$  are rotated by an angle  $\theta$  away from  $\langle 0\bar{1}10 \rangle$  and  $\langle 0001 \rangle$  directions, respectively. Figures 1(a) and 1(b) show this convention graphically for  $\text{B}_{\text{Si}}^0(k_b)$  with a broken B-C bond on the  $(2\bar{1}\bar{1}0)$  mirror plane and for  $\text{B}_{\text{Si}}^0(h_a)$ , respectively.

Ground-states  $\text{B}_{\text{Si}}^0(k_b)$  and  $\text{B}_{\text{Si}}^0(h_a)$  have a calculated main

$g$  tensor component  $g_3 \sim 2.002$  along the C radical, making an angle with the [0001] direction of  $\theta = 70^\circ$  and  $0^\circ$ , respectively (see also Fig. 1). The  $g$  tensors are nearly or perfectly axial for both static  $B_{\text{Si}}^0(k_b)$  and  $B_{\text{Si}}^0(h_a)$  structures, resulting from the conspicuous alignment of the spin density on the carbon radical as Fig. 3(a) clearly displays. The match with the measurements carried out at low temperature ( $T \lesssim 45$  K) is excellent, both in terms of magnitude (error  $\lesssim 0.0005$ ) and monoclinic angle (error  $\sim 1^\circ$ ). The error bar of the components perpendicular to the C-radical ( $g_1$  and  $g_2$ ) is about 4 times larger, but still, the agreement is deemed very good, especially considering that both calculated and observed  $g$  values show identical trends in terms of axial character and anisotropy:  $g_2 - g_1 = 0.0010$  for  $B_{\text{Si}}^0(k_b)$ , and  $g_3 - g_1 = -0.0067$  for  $B_{\text{Si}}^0(h_a)$ .

The calculated  $g$  tensor components of Tab. I were found by sampling the band structure over a  $2 \times 2 \times 2$  mesh of  $\mathbf{k}$ -points. A denser  $3 \times 3 \times 3$ -mesh calculation for  $B_{\text{Si}}^0(h_a)$  gave  $g_1 = g_2 = 2.0083$  and  $g_3 = 2.0015$ , which deviate from the results with the coarser mesh by 0.0007. Most importantly, the relative magnitude of the axial and transverse components is similar in both calculations and match very well the observations.

As discussed at the end of Sec. III A, the activation energy for rotation of the broken bond of  $B_{\text{Si}}^0(k_b)$  around [0001] was estimated at about 0.1 eV, allowing the structure to jump between all three equivalent alignments at rather low temperatures. This result is consistent with the observed raise of symmetry of the EPR signal assigned to shallow boron in cubic sites, from monoclinic to trigonal above  $T \sim 45$  K. We argue that above this temperature, the  $B_{\text{Si}}^0(k)$  defect jumps between three equivalent monoclinic configurations at a rate much faster than the inverse of the EPR recording time. The result is the observation of a “dynamic” state with effective  $C_{3v}$  symmetry (hereafter labeled with a “dyn” subscript), whose  $g$  tensor is estimated by averaging over all three equivalent  $C_{1h}$  orientations. The calculated axial component  $g_3 = 2.0073$  of  $B_{\text{Si}}^0(k_{\text{dyn}})$ , now along [0001], mostly inherits contributions from  $g_2 = 2.0078$  of static  $B_{\text{Si}}^0(k_b)$  configurations [see Fig. 1(a)], thus becoming the largest component. This contrasts with  $g_3$  of  $B_{\text{Si}}^0(h_a)$  which is the smallest component of this configuration. The magnitude of the calculated  $g$  values of  $B_{\text{Si}}^0(k_{\text{dyn}})$  agrees very well with those assigned to shallow boron on the cubic site measured in the temperature range  $T = 61\text{-}83$  K (error  $< 0.001$ ). The calculated anisotropy  $g_3 - g_1 \approx 0.002$  for  $B_{\text{Si}}^0(k_{\text{dyn}})$  differs from the measurements by 0.0004 only.

The coupling of the unpaired spin of  $B_{\text{Si}}^0$  defects with  $^{13}\text{C}$  and  $^{11}\text{B}$  magnetic isotopes quantifies the magnitude and shape of the spin density at the core of the defect.  $^{11}\text{B}$  and  $^{13}\text{C}$  hyperfine data was recorded experimentally at 3.4 K [26] and 1.5 K [28] by EPR and ENDOR, respectively. Under these conditions  $B_{\text{Si}}^0$  defects are static and the HF signals could be resolved. The calculated principal values of the HF tensors due to interactions with  $^{13}\text{C}$  and  $^{11}\text{B}$  elements at the broken C-B bond of  $B_{\text{Si}}^0$  defects ( $k_b$  and  $h_a$  structures) are reported in Tab. II. Also reported are the isotropic and anisotropic HF constants ( $a$  and  $b$ , respectively), which assume an axial character for the wave function of the unpaired electron. The upper and lower halves of the table show the results for boron

Table II. Calculated principal values of the hyperfine tensors ( $A_1$ ,  $A_2$  and  $A_3$ ) for  $^{13}\text{C}$  and  $^{11}\text{B}$  species located in the broken C-B bond of  $B_{\text{Si}}^0(k)$  and  $B_{\text{Si}}^0(h)$  defects in 4H-SiC. Isotropic and anisotropic HF constants ( $a$  and  $b$ ) are also shown and they assume an axial state pointing along direction 3. For the trigonal  $B_{\text{Si}}^0(h)$  defect, directions 1 and 2 are along the basal plane. For the monoclinic  $B_{\text{Si}}^0(k)$  defect,  $B_1$  is the component perpendicular to the  $\{2\bar{1}\bar{1}0\}$  mirror plane, while  $B_2$  and  $B_3$  are rotated by an angle  $\theta$  away from  $\langle 0\bar{1}10 \rangle$  and  $\langle 0001 \rangle$  directions, respectively (see Fig. 1). EPR data from  $^{13}\text{C}$ -enriched samples ( $^{13}\text{C}$ -EPR) [26] and  $^{11}\text{B}$ -ENDOR [28] are also included for comparison. These were obtained in 6H-SiC and pertain to boron defects at  $k_1$  ( $k_1$  and  $k_2$  data are very similar) and  $h$  sites. All HF couplings are in MHz.

Defect	$A_1$	$A_2$	$A_3$	$a$	$b$	$\theta$ ( $^\circ$ )
$^{13}\text{C}$ - $B_{\text{Si}}^0(k_b)$	34	34	183	84	50	72
$^{13}\text{C}$ -EPR [26]	48	48	169	88	40	$\sim 70$
$\text{C-}^{11}\text{B}_{\text{Si}}^0(k_b)$	0	0	6	2	2	74
$^{11}\text{B}$ -ENDOR [28]	-6.78	-6.78	2.40	-3.72	3.06	$\sim 70$
$^{13}\text{C}$ - $B_{\text{Si}}^0(h_a)$	30	30	182	81	51	0
$^{13}\text{C}$ -EPR [26]	48	48	173	90	42	0
$\text{C-}^{11}\text{B}_{\text{Si}}^0(h_a)$	2	2	8	4	2	0
$^{11}\text{B}$ -ENDOR [28]	-3.88	-3.88	4.85	-0.97	2.91	0

located on cubic and hexagonal sublattice sites, respectively. The experimental data accompanying the calculations relate to boron defects in 6H-SiC samples [26, 28].

The calculations confirm that the paramagnetic state is essentially axial along direction 3 (see principal directions and monoclinic angle  $\theta$  in Fig. 1). Differences between  $A_1$  and  $A_2$  were always lower than 1 MHz. Both theory and experiments indicate a relatively large and close  $^{13}\text{C}$  Fermi contact ( $a \sim 80\text{-}90$  MHz), reflecting the large localization on the C radical. The calculated anisotropic  $^{13}\text{C}$  HF constants ( $b \sim 50$  MHz) are also in fair agreement with the EPR data ( $b \sim 40$  MHz). Although not statistically meaningful, the error bar of the calculated HF constants (considering the measurements reported in Tab. II) is estimated as  $\lesssim 10$  MHz. We also note that the isotropic HF constants slightly underestimate previous calculations based on the local density approximation (LDA) [35]. This is interpreted as a tendency of GGA to underlocalize the electron density in comparison to the overlocalization of the LDA.

Regarding the  $^{11}\text{B}$  HF interactions, like their measured analogues, the amplitudes are very small (few MHz). Unlike the calculations, the measured Fermi contact is negative. Still, the discrepancy is well within the estimated error. Hence, along with the  $g$  tensors, the HF calculations provide compelling support for the assignment of  $B_{\text{Si}}^0$  to the EPR/ENDOR data as reproduced in Tabs. I and II.

The above HF interaction calculations were carried out using the GIPAW code within the GGA to the exchange-correlation potential. We performed test calculations at the HSE06 level (using the VASP code) and found that the Fermi

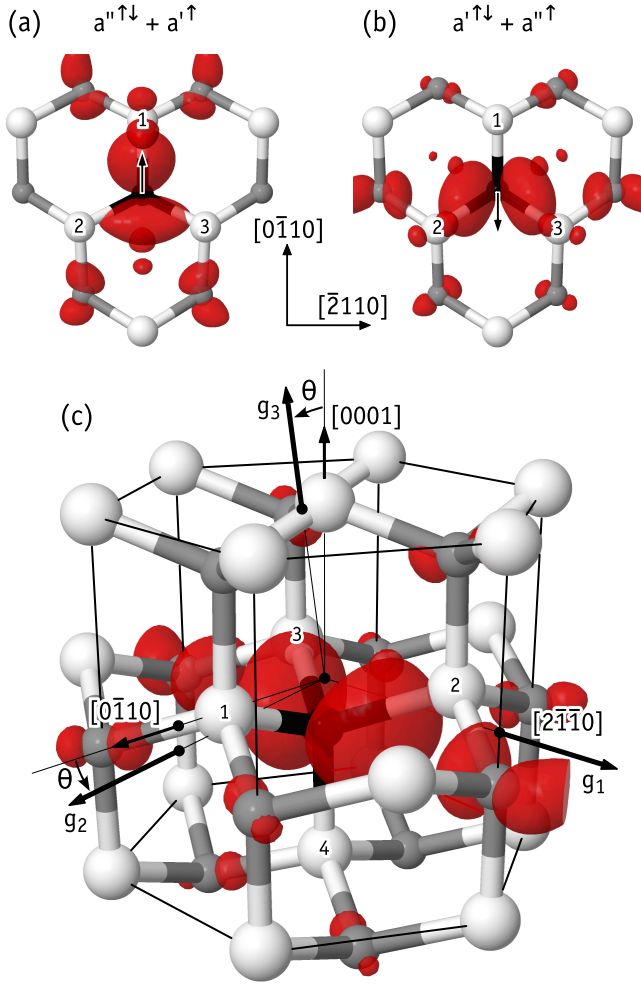


Figure 8. Spin-density isosurface (cutoff  $0.02 e/\text{\AA}^3$ ) of a neutral  $B_C$  defect at the  $k$  site of 4H-SiC. (a) and (b) depict two alternative Jahn-Teller distorted states, namely  $a''\uparrow\downarrow + a'\uparrow$  (metastable) and  $a'\uparrow\downarrow + a''\uparrow$  (ground state), which lead to opposite displacements of the B atom along  $[0\bar{1}\bar{1}0]$  (see arrows). In (c) we depict the  $a'\uparrow\downarrow + a''\uparrow$  ground state along with the principal directions of the calculated  $g$  tensor (see text). Si, C and B atoms are shown in white, gray and black, respectively.

contact terms were about a factor of two larger. The HSE06-level dipolar terms were similar to those found using the semilocal functional. Such discrepancy was also reported in Ref. [66] for the evaluation of isotropic coupling constant using semilocal and hybrid functionals, and that calls for further investigations.

Regarding the deep boron species, among the arguments behind its assignment to a  $B_{Si}-V_C$  structure were the negligible  $^{13}\text{C}$  and  $^{11}\text{B}$  hyperfine satellites next to the main signal, as well as a pronounced localization of the spin density on Si atoms [14, 15]. Unfortunately, the dynamic Jahn-Teller effect makes any comparison between the measurements and the static HF calculations rather difficult — unlike the Zeeman effect, the  $^{29}\text{Si}$  HF interactions are intermittent due to rotation of the nodal wave function.

We calculated the  $g$  tensor for neutral  $B_{Si}(k)-V_C^0(k)$ , with

both the B atom and the vacancy aligned along the crystalline main axis. The ground state structure involves an electronically-inert threefold coordinated B atom next to three Si radicals edging the C-vacancy, two of which reconstruct to form an elongated bond due to JT effect (see Ref. [15] and references therein). Most spin density of this complex is localized on a single Si dangling bond polarized toward the center of the vacancy and the B atom. Although the distance between B and the Si radical is approximately the separation between second neighbors of the crystal, Si radical states are rather extended in space. In fact, considering its symmetry and character, the paramagnetic state must have a finite amplitude on B atom, and that feature does not favor the  $B_{Si}-V_C^0$  model.

The calculated  $g$  tensor of  $B_{Si}-V_C^0$  allows us draw more definite conclusions. The static JT distorted state of  $B_{Si}(k)-V_C^0(k)$  with  $C_{1h}$  symmetry has a main  $g_3$  component along the Si dangling bond, which makes an angle of  $\theta = 78^\circ$  with  $[0001]$  — this was not observed at a temperature as low as  $T = 4$  K. Accordingly, two nearly axial EPR signals with a main axis along  $[0001]$  were reported [14]. The magnitude of the calculated  $g$  values also differ markedly from the observed ones. Even considering a dynamic JT state (with effective  $C_{3v}$  symmetry), the calculated effective  $g$  value of  $B_{Si}(k)-V_C^0(k_{\text{dyn}})$  along the  $c$  axis ( $g_3 = 2.0063$ ) is too small when compared to its measured counterpart ( $g_3 = 2.029$ ) [14].

In Sec III B it was shown that the paramagnetic state of  $B_C^0$  has spin-1/2, and that it derives from a partially occupied JT distorted  $e(xy)\uparrow\downarrow$  doublet. Also as detailed on the right hand side of Fig. 2, this manifold derives from the boron  $p_x p_y$  states, which are nodal on the boron atom as well as along the  $c$  axis. The spin density of the JT distorted configurations  $a''\uparrow\downarrow + a'\uparrow$  and  $a'\uparrow\downarrow + a''\uparrow$  is depicted in Figs. 8(a) and 8(b). Such a shape anticipates a very small spin localization on the B atom. For the  $a'\uparrow\downarrow + a''\uparrow$  ground state, the amplitude is zero on boron and high on two basal Si ligands ( $\text{Si}_2$  and  $\text{Si}_3$ ).

The spin density of the ground state  $a'\uparrow\downarrow + a''\uparrow$  configuration of  $B_C^0(k)$  is zoomed in Fig. 8(c). The case of  $B_C^0(h)$  is analogous and a similar discussion applies. The figure also depicts the principal directions of the  $g$  values with respect to the crystalline axes. Like it was considered for the shallow boron defect, trigonal ( $C_{3v}$ ) states have its main  $g_3$  component along the  $[0001]$  hexagonal axis. Also, monoclinic ( $C_{1h}$ ) states have  $g_1$  perpendicular to the  $\{2\bar{1}\bar{1}0\}$  plane, while  $g_2$  and  $g_3$  are rotated by an angle  $\theta$  away from  $\langle 0\bar{1}\bar{1}0 \rangle$  and  $\langle 0001 \rangle$ , respectively.

Let us first consider the case of static JT distorted configurations. These correspond to monoclinic states with calculated  $g$  values of  $g_1 \approx 2.005$ ,  $g_2 \approx 2.017\text{-}2.020$  and  $g_3 \approx 2.024\text{-}2.028$ . The latter is rotated away from  $[0001]$  by  $\theta = 13^\circ$  only. Although the magnitude of  $g_3$  is not far from the measured axial  $g$  values, the monoclinic rotation angle was not observed.

Considering that  $B_C^0$  is predicted to show a dynamic JT effect, the effective  $g$  values are better estimated via averaging over symmetrically equivalent alignments. Hence, we find  $g_1 = g_2 \approx 2.012$  for both  $B_C^0(k_{\text{dyn}})$  and  $B_C^0(h_{\text{dyn}})$ , whereas  $g_3 \approx 2.028$  and  $2.024$  for  $B_C^0(k_{\text{dyn}})$  and  $B_C^0(h_{\text{dyn}})$ , respectively. As reported in Tab. I, the calculated main  $g_3$  values are in ex-

cellent agreement with the axial  $g$  values observed for deep boron defects in 4H-SiC [14]. The basal  $g$  values also compare well with the corresponding measured figures ( $\sim 2.0$ ), although these are accompanied by relatively large error bars due to random  $g$ -strain broadening effects [15].

The nodal state shown in Fig. 8(c) strongly overlaps with two of the Si atoms connected to boron (Si<sub>2</sub> and Si<sub>3</sub>). The two other Si ligands are nodal (Si<sub>1</sub> and Si<sub>4</sub>) and have no overlap with the spin density. We suggest that the dynamic JT effect on this defect could be responsible for an intermittent localization on all atoms, thus explaining the weak and broad hyperfines detected for <sup>11</sup>B, <sup>13</sup>C, and <sup>29</sup>Si. Finally, we also note that the dynamical nature of the ground-state of B<sub>C</sub><sup>0</sup>, and a possible occupancy of both  $a''\uparrow\downarrow + a'\uparrow$  and  $a'\uparrow\downarrow + a''\uparrow$  states above few tens of degrees Kelvin, could explain the broadening and quenching of the EPR main signals of deep boron above  $T \approx 30$  K [14].

#### IV. CONCLUSIONS

We reported on first-principles hybrid density functional calculations of boron defects in 4H-SiC. Besides defect structures and electronic transition levels, defect free energies at finite temperatures,  $g$  tensor calculations and hyperfine coupling constants were also reported. The vibrational contribution to the free energies, as well as the one-electron states for the calculation of the paramagnetic properties, were found within a semilocal approximation to the electronic exchange and correlation interactions.

We support the assignment of the shallow boron species to B<sub>Si</sub>. In the neutral state, these defects possess a threefold coordinated B atom next to an unsaturated C radical. We mind the reader that this structure was obtained when the atomistic relaxation was performed within hybrid DFT. Lower level GGA calculations led to fourfold coordinated boron atoms. In line with arguments already reported [35], the erroneous GGA structure derives from the overmixing between the acceptor state of boron and the valence band top of the crystal. However, unlike Ref. [35], we conclude that the neutral B<sub>Si</sub> defect adopts a singlet state. The axially distorted structure of this defect (along the  $c$  axis) conserves the maximum point group symmetry of the 4H-SiC crystal ( $C_{3v}$ ). The displacement from the perfect lattice site can be explained by the host crystal field. Hence, the off-site structure cannot be justified by a Jahn-Teller effect — it is simply driven by the short covalent radius of boron compared to that of Si.

As a word of caution, we note that the relative energy of on-site and off-site B<sub>Si</sub><sup>0</sup> states cannot be easily obtained with the present method. If the fourfold coordinated B<sub>Si</sub><sup>0</sup> is a diffuse effective-mass-like state, it could be disfavored due to the artificial confinement effect of the supercell approximation [80]. Still, even if that was the case, only the off-site threefold coordinated B<sub>Si</sub><sup>0</sup> model (and not the EMT-model) could account for the measurements.

The C radicals on cubic and hexagonal B<sub>Si</sub> defects are polarized differently, *i.e.*, along basal and axial bond directions of the crystal, respectively. This feature has been previously

detected by EPR but left unexplained. We demonstrate that it results from distinct crystal fields acting on each sublattice site.

Substitutional boron on the carbon site (B<sub>C</sub><sup>0</sup>) is a dynamic Jahn-Teller system with a “Mexican hat” like potential. The potential ripples for rotation around the symmetry axis of the undisturbed state are 15 meV high only. This figure is lower than the zero-point energy of the defect, implying that it shows effective trigonal symmetry, even at liquid-helium temperature.

B<sub>Si</sub> and B<sub>C</sub> are both single acceptors. Despite adopting rather different alignments in the crystal, the acceptor levels of B<sub>Si</sub>( $k$ ) and B<sub>Si</sub>( $h$ ) are estimated in a narrow range  $E_v + (0.34-0.32)$  eV. This could explain the observation of a single transition by Laplace-DLTS for shallow boron. The acceptor level of B<sub>C</sub> is anticipated at  $E_v + (0.63-0.67)$  eV, in excellent agreement with the D-center transition level measured in the range 0.5-0.7 eV above  $E_v$ . Our results suggest that recently reported Laplace-DLTS experiments unfolding the D-center signal into two components, relate to a “shallower” configuration sitting at the cubic carbon site and a “deeper” one replacing the hexagonal site.

From the calculated free-energies of B<sub>Si</sub> and B<sub>C</sub>, we found that under typical growth temperatures, the equilibrium concentration ratio  $[B_{Si}]/[B_C] \approx 200$  and about 0.1 for a Si-poor and Si-rich stoichiometry, respectively. This leads us to the conclusion that formation of B<sub>C</sub> cannot be avoided during growth when boron is present, and contamination of n-type layers with boron could limit the mobility and lifetime of holes due to trapping and recombination at deep B<sub>C</sub> acceptors.

We demonstrated that the EPR measurements of shallow boron can be described by a site- and temperature-dependent  $g$  tensor of B<sub>Si</sub>. Below  $\sim 50$  K, neutral B<sub>Si</sub> defects at  $k$  and  $h$  sites show static  $C_{1h}$  and  $C_{3v}$  symmetry, with comparable  $g$  values along the carbon radical p-state, respectively  $g_3 = 2.0028$  and  $2.0022$ . These figures compare very well with  $2.0025$  and  $2.0019$  from the measurements, respectively. Above  $\sim 50$  K, the EPR signal related to the hexagonal species remains unchanged. However, the B-C broken bond in B<sub>Si</sub>( $k$ ) can reorient by surmounting a barrier of about 0.1 eV, and the estimated *thermally-averaged*  $g_3$  value (now parallel to [0001]) increases to  $2.0073$  (to be compared to  $2.0064$  from the measurements).

Calculations of the gyromagnetic tensor are complemented with calculations of the most prominent <sup>13</sup>C and <sup>11</sup>B hyperfine splitting interactions involving core atoms at the threefold coordinated B<sub>Si</sub><sup>0</sup> defects. The results agree well with the measurements both in terms of magnitude and axial direction of the interactions.

Our results rule against the assignment of a B<sub>Si</sub>-V<sub>C</sub> complex to the deep boron defect. Both directions and magnitude of the calculated  $g$  values for this complex, differ markedly from the observations. Combining with previous calculations which concluded that B<sub>Si</sub>-V<sub>C</sub> is a donor without levels in the lower half of the gap [17], we can definitely abandon the idea of a relation between the deep boron center and B<sub>Si</sub>-V<sub>C</sub>.

Instead we assign deep boron to B<sub>C</sub>. The calculated  $g$  val-

ues for  $B_C$  show excellent agreement with the measurements for deep boron if we account for the dynamics of the defect. We argue that the dynamic Jahn-Teller effect, along with the nodal shape of the paramagnetic state, could explain the weak and broad hyperfine signals related to  $^{11}\text{B}$ ,  $^{13}\text{C}$  and  $^{29}\text{Si}$ . Additionally, by considering  $B_C$  as being responsible for the deep boron spectra, and hence ruling out the  $B_{Si}-V_C$  model, we naturally avoid having to justify the inexplicable formation of  $B_{Si}-V_C$  defects with exclusive axial orientations as observed by EPR.

## DATA AVAILABILITY STATEMENT

The data that support the findings of this study are available from the corresponding author upon reasonable request.

## ACKNOWLEDGMENTS

The present work was supported by the NATO Science for Peace and Security Programme, project no. G5674. JC and VJBT acknowledge the FCT through projects LA/P/0037/2020, UIDB/50025/2020 and UIDP/50025/2020.

- 
- [1] T. Kimoto and J. A. Cooper, *Fundamentals of silicon carbide technology* (John Wiley & Sons, Singapore, 2014).
- [2] G. Liu, B. R. Tuttle, and S. Dhar, *Applied Physics Reviews* **2**, 021307 (2015).
- [3] J. Coutinho, V. J. B. Torres, I. Capan, T. Brodar, Z. Ereš, R. Bernat, V. Radulović, K. Ambrožič, L. Snoj, Ž. Pastuović, A. Sarbutt, T. Ohshima, Y. Yamazaki, and T. Makino, *Nuclear Instruments and Methods in Physics Research Section A: Accelerators, Spectrometers, Detectors and Associated Equipment* **986**, 164793 (2021).
- [4] D. M. Lukin, C. Dory, M. A. Guidry, K. Y. Yang, S. D. Mishra, R. Trivedi, M. Radulaski, S. Sun, D. Verduyck, G. H. Ahn, and J. Vučković, *Nature Photonics* **14**, 330 (2019).
- [5] S. Castelletto and A. Boretti, *Journal of Physics: Photonics* **2**, 022001 (2020).
- [6] G. Wolfowicz, F. J. Heremans, C. P. Anderson, S. Kanai, H. Seo, A. Gali, G. Galli, and D. D. Awschalom, *Nature Reviews Materials* **6**, 906 (2021).
- [7] C. P. Anderson, E. O. Glen, C. Zeledon, A. Bourassa, Y. Jin, Y. Zhu, C. Vorwerk, A. L. Crook, H. Abe, J. Ul-Hassan, T. Ohshima, N. T. Son, G. Galli, and D. D. Awschalom, *Science Advances* **8**, abm5912 (2022).
- [8] W. Suttrop, G. Pensl, and P. Lanig, *Applied Physics A Solids and Surfaces* **51**, 231 (1990).
- [9] S. G. Sridhara, L. L. Clemen, R. P. Devaty, W. J. Choyke, D. J. Larkin, H. S. Kong, T. Troffer, and G. Pensl, *Journal of Applied Physics* **83**, 7909 (1998).
- [10] Y. Gao, S. I. Soloviev, and T. S. Sudarshan, *Applied Physics Letters* **83**, 905 (2003).
- [11] M. Bockstedte, A. Mattausch, and O. Pankratov, *Physical Review B* **70**, 115203 (2004).
- [12] O. V. Aleksandrov and E. N. Mokhov, *Materials Science Forum* **740-742**, 561 (2013).
- [13] H. Kuwabara and S. Yamada, *Physica Status Solidi (a)* **30**, 739 (1975).
- [14] P. G. Baranov, I. V. Il'in, and E. N. Mokhov, *Physics of the Solid State* **40**, 31 (1998).
- [15] A. v. Duijn-Arnold, T. Ikoma, O. G. Poluektov, P. G. Baranov, E. N. Mokhov, and J. Schmidt, *Physical Review B* **57**, 1607 (1998).
- [16] M. Bockstedte, A. Mattausch, and O. Pankratov, *Materials Science Forum* **353-356**, 447 (2001).
- [17] B. Aradi, A. Gali, P. Deák, E. Rauls, T. Frauenheim, and N. T. Son, *Materials Science Forum* **353-356**, 455 (2001).
- [18] L. Storasta, P. Bergman, E. Janzén, and C. Hallin, *Materials Science Forum* **389-393**, 549 (2002).
- [19] K. Kawahara, J. Suda, and T. Kimoto, *Journal of Applied Physics* **113**, 033705 (2013).
- [20] T. Okuda, G. Alfieri, T. Kimoto, and J. Suda, *Applied Physics Express* **8**, 111301 (2015).
- [21] H. M. Ayyedh, N. Iwamoto, R. Nipoti, A. Hallén, and B. G. Svensson, *Materials Science Forum* **897**, 262 (2017).
- [22] A. V. Bolotnikov, P. G. Muzykov, A. E. Grekov, and T. S. Sudarshan, *IEEE Transactions on Electron Devices* **54**, 1540 (2007).
- [23] A. Yang, K. Murata, T. Miyazawa, T. Tawara, and H. Tsuchida, *Journal of Applied Physics* **126**, 055103 (2019).
- [24] M. M. Anikin, A. A. Lebedev, A. L. Syrkin, and A. V. Suvorov, *Fiz. Tekh. Poluprovodn.* **19**, 114 (1985), [*Sov. Phys. Semicond.* **15**, 69 (1985)].
- [25] I. Capan, T. Brodar, Y. Yamazaki, Y. Oki, T. Ohshima, Y. Chiba, Y. Hijikata, L. Snoj, and V. Radulović, *Nuclear Instruments and Methods in Physics Research Section B: Beam Interactions with Materials and Atoms* **478**, 224 (2020).
- [26] A. G. Zubatov, I. M. Zaritzkii, S. N. Lukin, E. N. Mokhov, and V. G. Stepanov, *Soviet Physics Solid State* **27**, 2085 (1985).
- [27] R. Muller, M. Feege, S. Greulich-Weber, and J.-M. Spaeth, *Semiconductor Science and Technology* **8**, 1377 (1993).
- [28] T. Matsumoto, O. G. Poluektov, J. Schmidt, E. N. Mokhov, and P. G. Baranov, *Physical Review B* **55**, 2219 (1997).
- [29] S. Greulich-Weber, *physica status solidi (a)* **162**, 95 (1997).
- [30] S. Greulich-Weber, F. Feege, K. N. Kalabukhova, S. N. Lukin, J.-M. Spaeth, and F. J. Adrian, *Semiconductor Science and Technology* **13**, 59 (1998).
- [31] V. Y. Bratus, N. P. Baran, A. A. Bugai, A. A. Klimov, V. M. Maksimenko, T. L. Petrenko, and V. Romanenko, *Defect and Diffusion Forum* **103-105**, 645 (1993).
- [32] T. L. Petrenko, V. V. Teslenko, A. A. Bugai, V. D. Khavryutchenko, and A. A. Klimov, *Semiconductor Science and Technology* **11**, 1276 (1996).
- [33] A. Fukumoto, *Physical Review B* **53**, 4458 (1996).
- [34] P. Deák, B. Aradi, A. Gali, U. Gerstmann, and W. J. Choyke, *Materials Science Forum* **433-436**, 523 (2003).
- [35] U. Gerstmann, A. Gali, P. Deák, T. Frauenheim, and H. Overhof, *Materials Science Forum* **457-460**, 711 (2004).
- [36] T. Oda, Y. Zhang, and W. J. Weber, *The Journal of Chemical Physics* **139**, 124707 (2013).
- [37] G. Kresse and J. Hafner, *Physical Review B* **47**, 558 (1993).
- [38] G. Kresse and J. Hafner, *Physical Review B* **49**, 14251 (1994).
- [39] G. Kresse and J. Furthmüller, *Computational Materials Science* **6**, 15 (1996).
- [40] G. Kresse and J. Furthmüller, *Physical Review B* **54**, 11169 (1996).

- [41] P. E. Blöchl, *Physical Review B* **50**, 17953 (1994).
- [42] J. Heyd, G. E. Scuseria, and M. Ernzerhof, *The Journal of Chemical Physics* **118**, 8207 (2003).
- [43] A. V. Krukau, O. A. Vydrov, A. F. Izmaylov, and G. E. Scuseria, *The Journal of Chemical Physics* **125**, 224106 (2006).
- [44] J. P. Perdew, K. Burke, and M. Ernzerhof, *Physical Review Letters* **77**, 3865 (1996).
- [45] P. Grivickas, V. Grivickas, J. Linnros, and A. Galeckas, *Journal of Applied Physics* **101**, 123521 (2007).
- [46] M. Stockmeier, R. Müller, S. A. Sakwe, P. J. Wellmann, and A. Magerl, *Journal of Applied Physics* **105**, 033511 (2009).
- [47] J. D. Gouveia and J. Coutinho, *Electronic Structure* **1**, 015008 (2019).
- [48] G.-X. Qian, R. M. Martin, and D. J. Chadi, *Physical Review B* **38**, 7649 (1988).
- [49] J. Coutinho, V. P. Markevich, and A. R. Peaker, *Journal of Physics: Condensed Matter* **32**, 323001 (2020).
- [50] C. Freysoldt, J. Neugebauer, and C. G. Van de Walle, *Physical Review Letters* **102**, 016402 (2009).
- [51] Y. Kumagai and F. Oba, *Physical Review B* **89**, 195205 (2014).
- [52] J. Coutinho, V. J. B. Torres, K. Demmouche, and S. Öberg, *Physical Review B* **96**, 174105 (2017).
- [53] See Supplemental Material at <http://link.aps.org/supplemental/10.1103/PhysRevB.106.224112> for details regarding convergence tests, defect geometries, calculation of energy barriers, justification of the overmixing effect, and hole capture mechanism of  $\text{B}_{\text{Si}}$ .
- [54] G. Makov and M. C. Payne, *Physical Review B* **51**, 4014 (1995).
- [55] C. W. M. Castleton, A. Höglund, and S. Mirbt, *Physical Review B* **73**, 035215 (2006).
- [56] S. Lany and A. Zunger, *Physical Review B* **78**, 235104 (2008).
- [57] E. Greenberg, C. A. Natke, and W. N. Hubbard, *The Journal of Chemical Thermodynamics* **2**, 193 (1970).
- [58] M. Widom and M. Mihalkovič, *Physical Review B* **77**, 064113 (2008).
- [59] S. K. Estreicher, M. Sanati, D. West, and F. Ruymgaart, *Physical Review B* **70**, 125209 (2004).
- [60] D. Murali, M. Posselt, and M. Schiwarth, *Physical Review B* **92**, 064103 (2015).
- [61] D. Gomes, V. P. Markevich, A. R. Peaker, and J. Coutinho, *Physica Status Solidi B* , 2100670 (2022).
- [62] C. J. Pickard and F. Mauri, *Physical Review Letters* **88**, 086403 (2002).
- [63] P. Giannozzi, S. Baroni, N. Bonini, M. Calandra, R. Car, C. Cavazzoni, D. Ceresoli, G. L. Chiarotti, M. Cococcioni, I. Dabo, A. D. Corso, S. de Gironcoli, S. Fabris, G. Fratesi, R. Gebauer, U. Gerstmann, C. Gougoussis, A. Kokalj, M. Lazzeri, L. Martin-Samos, N. Marzari, F. Mauri, R. Mazzarello, S. Paolini, A. Pasquarello, L. Paulatto, C. Sbraccia, S. Scandolo, G. Sclauzero, A. P. Seitsonen, A. Smogunov, P. Umari, and R. M. Wentzcovitch, *Journal of Physics: Condensed Matter* **21**, 395502 (2009).
- [64] P. Giannozzi, O. Andreussi, T. Brumme, O. Bunau, M. Buongiorno Nardelli, M. Calandra, R. Car, C. Cavazzoni, D. Ceresoli, M. Cococcioni, N. Colonna, I. Carnimeo, A. Dal Corso, S. de Gironcoli, P. Delugas, R. A. DiStasio, A. Ferretti, A. Floris, G. Fratesi, G. Fugallo, R. Gebauer, U. Gerstmann, F. Giustino, T. Gorni, J. Jia, M. Kawamura, H.-Y. Ko, A. Kokalj, E. Küçükbenli, M. Lazzeri, M. Marsili, N. Marzari, F. Mauri, N. L. Nguyen, H.-V. Nguyen, A. Otero-de-la-Roza, L. Paulatto, S. Poncé, D. Rocca, R. Sabatini, B. Santra, M. Schlipf, A. P. Seitsonen, A. Smogunov, I. Timrov, T. Thonhauser, P. Umari, N. Vast, X. Wu, and S. Baroni, *Journal of Physics: Condensed Matter* **29**, 465901 (2017).
- [65] C. J. Pickard and F. Mauri, *Physical Review B* **63**, 245101 (2001).
- [66] D. Skachkov, W. R. L. Lambrecht, H. J. von Bardeleben, U. Gerstmann, Q. D. Ho, and P. Deák, *Journal of Applied Physics* **125**, 185701 (2019).
- [67] C. G. V. de Walle and P. E. Blöchl, *Physical Review B* **47**, 4244 (1993).
- [68] H. J. Monkhorst and J. D. Pack, *Physical Review B* **13**, 5188 (1976).
- [69] P. A. Schultz, R. M. V. Ginhoven, and A. H. Edwards, *Physical Review B* **103**, 195202 (2021).
- [70] M. Bockstedte, A. Mattausch, and O. Pankratov, *Physical Review B* **68**, 205201 (2003).
- [71] P. Deák, A. Gali, J. Miró, R. Gutierrez, A. Sieck, and T. Frauenheim, *Materials Science Forum* **264-268**, 279 (1998).
- [72] W. V. Smith, P. P. Sorokin, I. L. Gelles, and G. J. Lasher, *Physical Review* **115**, 1546 (1959).
- [73] M. Bockstedte, A. Mattausch, and O. Pankratov, *Applied Physics Letters* **85**, 58 (2004).
- [74] R. Jones, J. P. Goss, and P. R. Briddon, *Physical Review B* **80**, 033205 (2009).
- [75] G. Henkelman, B. P. Uberuaga, and H. Jónsson, *The Journal of Chemical Physics* **113**, 9901 (2000).
- [76] Malcolm W. Chase, Jr., in *Journal of Physical and Chemical Reference Data* (ACS, AIP and NIST, New York, 1998) 4th ed.
- [77] A. M. Stoneham, J. Gavartin, A. L. Shluger, A. V. Kimmel, D. M. Ramo, H. M. Rønnow, G. Aeppli, and C. Renner, *Journal of Physics: Condensed Matter* **19**, 255208 (2007).
- [78] A. M. Stoneham, *Reports on Progress in Physics* **44**, 1251 (1981).
- [79] A. Alkauskas, P. Broqvist, and A. Pasquarello, *Physical Review Letters* **101**, 046405 (2008).
- [80] L.-W. Wang, *Journal of Applied Physics* **105**, 123712 (2009).
- [81] A. Alkauskas, J. L. Lyons, D. Steiauf, and C. G. V. de Walle, *Physical Review Letters* **109**, 267401 (2012).
- [82] A. Alkauskas, M. D. McCluskey, and C. G. V. de Walle, *Journal of Applied Physics* **119**, 181101 (2016).
- [83] M. Ito, L. Storasta, and H. Tsuchida, *Applied Physics Express* **1**, 015001 (2008).

# Theory of shallow and deep boron defects in 4H-SiC

(Supplemental Material to Physical Review B 106, 224112 (2022); DOI:10.1103/PhysRevB.106.224112)

Vitor J. B. Torres,<sup>1</sup> Ivana Capan,<sup>2</sup> and José Coutinho<sup>1</sup>

<sup>1</sup>*I3N, Department of Physics, University of Aveiro, Campus Santiago, 3810-193 Aveiro, Portugal*

<sup>2</sup>*Ruder Bošković Institute, Bijenicka 54, 10000 Zagreb, Croatia*

## I. CONVERGENCE OF RESULTS WITH THE BOUNDARY CONDITIONS

First-principles point defect calculations commonly rely on the supercell approach, implying the use of periodic boundary conditions. Due to the neutralization condition and limited size of the supercells, the energy of charged defects is affected by sizable artificial interactions involving an infinite array of charges trapped at the defects implicitly present on every cell image, plus that of an explicit or implicit neutralizing background charge. In order to remove these unwanted interactions, several methods have been proposed (see for instance Refs. [50, 51, 54, 56, 69]). We use the recipe of Kumagai and Oba (KO) [51], which generalizes the method of Freysoldt, Neugebauer, and Van de Walle [50] for anisotropic materials like 4H-SiC. Previous tests to the KO method, using the double positive carbon vacancy ( $V_C^{2+}$ ) in 4H-SiC as case study, found that corrected formation energies were affected by an error bar below 20 meV for cells with few hundred atoms [52].

We know however, that the accuracy of such corrections (for a specific supercell size) depends on the shape and extent of the acceptor/donor states [36, 51, 69]. For that reason, we report below a set of tests pertaining the convergence of the formation energy of  $B_{Si}^-(h)$  in 4H-SiC using supercells of several sizes. We note that we are dealing with a singly negative point defect and that the correction varies with  $q^2$ , where  $q$  is the net charge of the defect [54].

Supercells with the following geometries were employed:  $4 \times 4 \times 2$  (256);  $5 \times 5 \times 2$  (400);  $6 \times 6 \times 3$  (864);  $8 \times 8 \times 4$  (2048) and  $10 \times 10 \times 4$  (3200). Here, the  $l \times m \times n$  triplets represent the unit cell replication factors and the figure within parentheses are the corresponding total number of atoms. We define the effective supercell size as  $L = V^{1/3}$ , where  $V$  is the total volume. The sampling of the Brillouin zones was carried out over  $\Gamma$ -centered  $2 \times 2 \times 2$  and  $1 \times 1 \times 1$  grids for the two smaller and three larger cells, respectively. Further details (including the calculation of chemical potentials) are described in the paper.

Figure 1 depicts the results of the convergence tests to the formation energy of  $B_{Si}^-(h)$  in C-rich 4H-SiC as a function of  $1/L$ . The red crosses represent the uncorrected formation energies. The red line is a fit of a function of the type  $aL^{-1} + bL^{-3} + c$  to the data [55]. The leading term accounts for the monopole correction, whereas

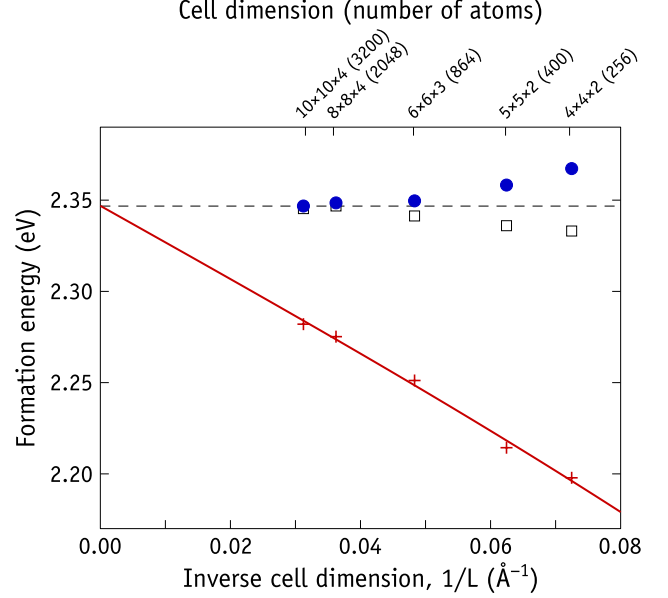


Figure 1. Convergence test to the formation energy of  $B_{Si}^-(h)$  in 4H-SiC. The upper horizontal axis indicates the  $m \times m \times n$  unit cell replication factors that correspond to the supercells used, along with the corresponding total number of atoms within parentheses. The lower horizontal axis is the inverse of the cell dimension  $L^{-1} = V^{-1/3}$ , where  $V$  is the volume of the supercell. Crosses represent the bare (uncorrected) formation energies, open squares are formation energies corrected by the simplest point charge correction of Makov and Payne [54], and closed circles represent formation energies corrected with the KO method [51].

the term in  $L^{-3}$  mostly accounts for dipole and elastic interactions. The constant  $c = 2.35$  eV is the extracted asymptotic formation energy for  $L \rightarrow \infty$ , represented by the horizontal dashed line in Fig. 1. We can readily note that the fit is nearly linear, to large extent suggesting that the error can be accounted for by a monopole correction. This is confirmed by the calculated formation energies with a point charge correction as proposed by Makov and Payne [54], shown in Fig. 1 as open squares. For the 400-atom supercells used in this work the difference to the asymptotic value is about 10 meV. These results are interpreted in the following way:  $B_{Si}^-$  is a substitutional anion, where the extra electron is mostly localized on the first neighboring B-C bonds. Hence, it is not surprising that it can be nearly described as a negative point charge.

Fig. 1 also shows the formation energies with the KO correction as a function of the supercell size (filled cir-



Table I. Calculated first ( $B-X_1$ ) and second ( $B-X_2$ ) neighbor distances to the B atom in substitutional boron defects replacing Si and C sites of 4H-SiC. Results using both PBE and HSE06 functionals are listed. All distances are in Å.

Defect	$B-X_1$		$B-X_2$	
	PBE	HSE06	PBE	HSE06
$B_{Si}^0(k)$	1.73	1.65	1.75	2.41
$B_{Si}^0(h)$	1.75	1.65	1.75	2.43
$B_{Si}^-(k)$	1.75	1.76	1.75	1.76
$B_{Si}^-(h)$	1.75	1.76	1.76	1.77
$B_C^0(k)$	1.92	1.92	1.95	1.98
$B_C^0(h)$	1.92	1.92	1.94	1.97
$B_C^-(k)$	1.90	1.90	1.90	1.91
$B_C^-(h)$	1.90	1.90	1.91	1.91

cles). The KO-corrected formation energies slightly overshoot the asymptotic value. For the 400-atom cells, the point charge and KO corrections to the negatively charged supercell energies are 0.12 eV and 0.14 eV, respectively. From the above, we estimate that the periodic boundary conditions induce an error bar of  $\sim 20$  meV to the calculated (KO-corrected) formation energies.

## II. DEFECT GEOMETRIES

In Tab. I we list the first and second neighbor distances to the B atom in substitutional boron defects in 4H-SiC. PBE relaxations were carried out with a  $\Gamma$ -centered  $2 \times 2 \times 2$  sampling mesh, whereas  $\Gamma$  sampling was done for the HSE06 relaxations.

In Ref. [36] it was found that defect structures obtained using  $\Gamma$  sampling on 216-atom cells, could be sensitive upon increasing the density of the mesh. Ref. [47] reports that for the case of neutral carbon interstitial in 3C-SiC, the PBE relaxed structure (and spin state) were incorrect due to mixing of defect states with the conduction band.

To investigate the reliability of the  $\Gamma$ -sampled 400-atom structures obtained within HSE06, we can inspect the atomistic geometries for the GIPAW calculations (HF splittings and  $g$  tensor), which were evaluated within HSE06 in 256-atom supercells using  $\Gamma$ -centered  $2 \times 2 \times 2$   $\mathbf{k}$  point grids (see Sec. II of the paper). The resulting structures and relative energies were essentially identical to those found from the  $\Gamma$ -sampled calculations. For instance, first and second B-C neighboring distances for the offsite  $B_{Si}^0(h)$  ground state were 1.65 and 2.45 Å. For  $B_{Si}^0(k)$ , the analogous distances are 1.65 and 2.42 Å. These figures are very close to the structural parameters reported in Tab. I.

We also carried out a batch of tests where we started from the  $B_{Si}^0(h)$  ground state structure obtained in 400-atom cells using  $\Gamma$  sampling and HSE06, and performed a

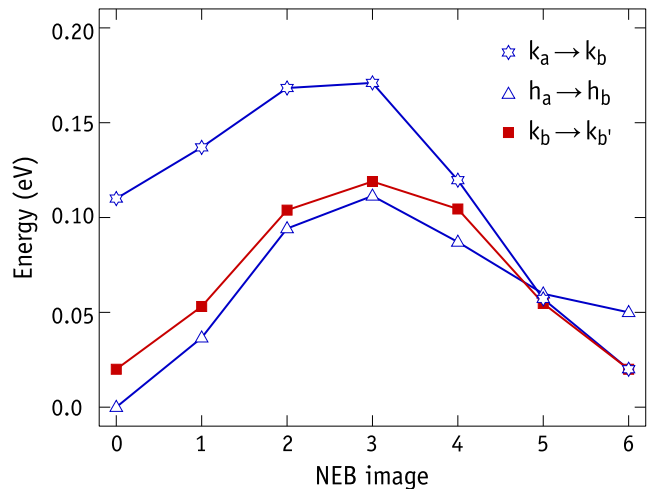


Figure 2. Minimum energy paths for boron motion in  $B_{Si}^0$  between the stable/metastable structures indicated in the legend. Calculations were performed using the climbing image nudged elastic band method [75]. Open symbols correspond to reorientations mechanisms from axial to basal offsite configurations. Filled squares correspond to the reorientation of  $B_{Si}^0(k)$  between two neighboring basal distortions. All mechanisms consider 5 intermediate images between the endpoints.

PBE-level relaxation using different  $\mathbf{k}$  point meshes. The tests considered  $\Gamma$ -centered  $2 \times 2 \times 2$  and  $4 \times 4 \times 4$ , as well as Monkhorst and Pack ( $\Gamma$ -free)  $2 \times 2 \times 2$  and  $4 \times 4 \times 4$  grids [68]. All these calculations provide the same incorrect answer, *i.e.*, the final structure is a fourfold coordinated  $B_{Si}$  defect without a carbon radical.

## III. REORIENTATION OF NEUTRAL $B_{Si}$

Here we provide the details behind the calculation of the barriers considered in the configuration coordinate diagram of Fig. 1(c) of the paper. They pertain to the reorientation of  $B_{Si}^0$  between offsite configurations in both  $k$  and  $h$  sublattice sites ( $k_a \rightarrow k_b$  and  $h_a \rightarrow h_b$ ). We also detail the calculation of the minimum energy path for the reorientation of  $B_{Si}^0(k)$  between two neighboring (symmetry equivalent) offaxis basal configurations ( $k_b \rightarrow k_{b'}$ ). This figure is relevant for understanding the temperature dependence of the electron paramagnetic resonance data (see Sec. III.E of the paper).

The reorientation mechanisms were investigated using the climbing image nudged elastic band method (CI-NEB) [75]. Essentially, we started with a guessed sequence by setting up an array of 400-atom supercell structures, comprising five intermediate structures linearly interpolated between the stable end-configurations. On a second step, a CI-NEB relaxation was performed with forces calculated at the HSE06 level and using the  $\Gamma$ -point for sampling the BZ. In a final step, the energies of the relaxed sequence of images were further refined by

improving the  $\mathbf{k}$  point sampling to  $\Gamma$ -centered  $2 \times 2 \times 2$  and performing single-point energy calculations at the HSE06 level.

Figure 2 shows the result of the NEB calculations referred above. At the ends (horizontal axis coordinates 0 and 6) we find ground states for each sublattice location ( $k_b$ ,  $h_a$  and  $k_{b'}$ ) and metastable states ( $k_a$  and  $h_b$ ) of off-site  $B_{Si}^0$  defects. All energies are represented with respect to the lowest energy  $B_{Si}^0(h_a)$  state. From the data we find activation barriers of 0.06 eV and 0.11 eV for  $k_a \rightarrow k_b$  and  $h_a \rightarrow h_b$  reorientations, respectively. A reorientation barrier of 0.09 eV is found for the  $k_b \rightarrow k_{b'}$  jump of  $B_{Si}^0(k)$ .

#### IV. OVERMIXING OF THE SHALLOW BORON ACCEPTOR WITH THE VALENCE BAND WITHIN PBE

Here we justify our argument regarding the existence of an overestimated and spurious mixing effect found at the PBE level, between the lowest unoccupied state of  $B_{Si}^0$  with the valence band of 4H-SiC. In Fig. 3(a) we depict two sequences of single-point total energies of  $B_{Si}^0(h)$  defects in 4H-SiC. They are both represented as a function of a reaction coordinate  $R$ , where atomic coordinates  $\mathbf{R} = \mathbf{R}_{HSE06}(1 - R) + \mathbf{R}_{PBE}R$  are linearly interpolated between ground state coordinates of  $B_{Si}^0(h)$  at HSE06 ( $R = 0$ , offsite structure) and PBE level (onsite structure). The calculations were spin polarized, used 400-atom supercells and  $\Gamma$ -centered  $2 \times 2 \times 2$  grids for the BZ sampling. For each functional, the origin of the energy scale is set to the respective ground state structure.

As expected, the red line in Fig. 3(a) joining the sequence of PBE energies, shows a clear minimum at  $R = 1$  ( $\mathbf{R}_{PBE}$ ) while the offsite  $\mathbf{R}_{HSE06}$  configuration is not stable. This was confirmed upon structural relaxation of the  $\mathbf{R}_{HSE06}$  coordinates within PBE. In Sec. II of this document, we shown that this is not an artifact and does not change upon improving the  $\mathbf{k}$  point sampling.

Conversely, at the HSE06 level (blue line), the minimum energy is at  $R = 0$  ( $\mathbf{R}_{HSE06}$ ) and the  $\mathbf{R}_{PBE}$  structure is metastable by nearly 0.1 eV. A relaxation of the onsite  $\mathbf{R}_{PBE}$  structure at the HSE06 level resulted in a local minimum (also four fold coordinated boron) 0.06 eV above the relaxed ground state  $R = 0$ .

Let us now look at the band structure change along the coordinate  $R$ . This is shown in Fig. 3(b). Line colors and labels are in direct correspondence with Fig. 3(a). We note that the valence band maxima of 4H-SiC within PBE lies  $\Delta E_v = 0.63$  eV above that of HSE06 (both shown as horizontal dashed lines). We are using the same pseudopotentials in the semilocal and hybrid calculations. Under these conditions, the macroscopically averaged PBE- and HSE06-level electrostatic potentials across the bulk are almost identical. Hence,  $\Delta E_v$  could be trivially found from the difference in the valence band

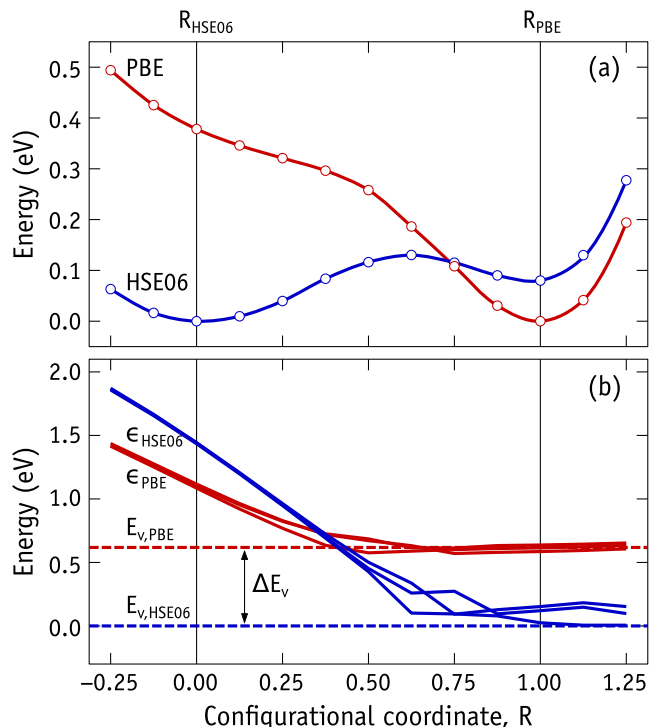


Figure 3. Analysis of neutral  $B_{Si}$  in 4H-SiC as a function of a configurational coordinate  $R$  (see text), using semilocal (PBE) and hybrid (HSE06) density functional theory. (a) Total energies of  $B_{Si}^0(h)$  defects at several  $R$  coordinates using PBE (red) and HSE06 (blue) functionals. The origin of the energy scale of each plot corresponds to the respective minimum energy structure. (b) Lowest unoccupied Kohn-Sham states of  $B_{Si}^0(h)$  in 4H-SiC using PBE and HSE06 functionals ( $\epsilon_{PBE}$  and  $\epsilon_{HSE06}$ , respectively). A total of three Kohn-Sham states are represented calculation, corresponding to three different  $\mathbf{k}$  points. The dashed lines represent the valence band top energy as found from the highest occupied Kohn-Sham state in a bulk supercell (using the appropriate functional). All energies are relative to  $E_{v,HSE06}$ . PBE data (red) is shifted from the HSE06 data (blue) by a valence band offset  $\Delta E_v = 0.63$  eV (see text).

maxima eigenvalues [78]. This operation, although not strictly necessary, has been carried out for the sake of clarity of the figure.

The energy of the lowest unoccupied state of  $B_{Si}^0(h)$  is represented along  $R$  by the solid lines. For each calculation, a total of three energies are represent and they stand for eigenvalues at three different  $\mathbf{k}$  points. This gives us an idea of the band dispersion for this level as a function of defect geometry. Importantly, for all structures, the highest occupied state (spin-up channel) has the character of the valence band and its localization spans across the supercell. Any spin-up B-related occupied state must be located below  $E_v$ .

It is clear that for both functionals, the lowest unoccupied state is high in the gap for the offsite  $\mathbf{R}_{HSE06}$  configuration. On the other hand, inspection of the highest occupied and lowest unoccupied states for the  $\mathbf{R}_{PBE}$  con-

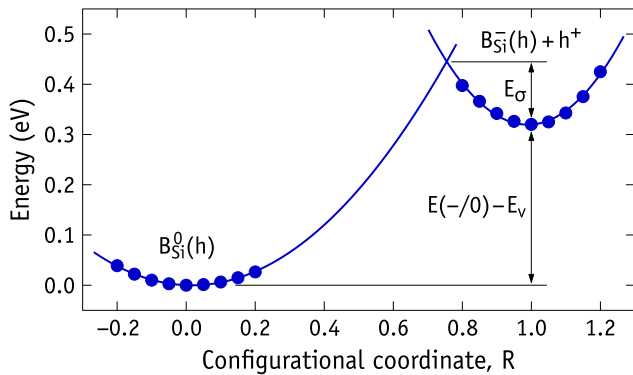


Figure 4. Potential energy surface along a linear path joining ground state structures of  $B_{Si}^0(h)$  (with  $R = 0$ ) and  $B_{Si}^-(h)$  (with  $R = 1$ ). Solid lines represent parabolic fits to the data in the vicinity of the respective minima.

figuration (within both PBE and HSE06) confirms that they are both delocalized and resemble a valence band state. In other words, as we go from threefold to fourfold coordination of boron, the unoccupied deep gap state of the offsite configuration *submerges* into the valence band, becoming occupied and leaving a hole at the top of the valence band.

Like for any gap state, the HSE approximation also mixes the boron state with the band edges. That is particularly evident for the  $\mathbf{R}_{PBE}$  structure, where a fourth B-C bond is formed. However, while the relevant gap state of the  $\mathbf{R}_{HSE06}$  geometry is nearly 1.5 eV above  $E_v$  within HSE-level DFT (this is about mid gap), within PBE the same structure shows a gap state which is less than 0.5 eV above the corresponding  $E_v$  level. This allows for less mixing in the correct HSE result, and more band mixing in the flawed PBE calculation.

While PBE suggests that  $B_{Si}$  in 4H-SiC is an effective mass theory (EMT) like acceptor, HSE06 results point for a deep hole trap (with a level about 0.3 eV above  $E_v$ ). These conclusions are also in line with the staggering difference between the spin density of threefold and fourfold coordinated  $B_{Si}^0(h)$  defects (see Figs 3(a) and 3(b) of the paper). Unlike the PBE diffuse spin density, within HSE06 the density is strongly localized on the nearest shells of atoms around B, most notably on the C radical next to boron.

## V. HOLE CAPTURE MECHANISM OF $B_{Si}$

The  $B_{Si}^-$  defect does not have deep states in the gap — it is a fourfold coordinated isovalent anion whose negative charge is localized on its four B-C bonds. It is possible that this state could attract free holes and hold them

with a small EMT like binding energy. Indeed as indicated in Fig. 3, the onsite structure of  $B_{Si}^0$  is metastable. Our method is not the best to estimate meV-accurate effective mass hole binding energies. That would require many thousands of atoms in the supercell [79]. However, judging from the experimental and calculated spectroscopic properties of  $B_{Si}$ , the neutral ground state is the offsite threefold coordinated structure. An eventual onsite  $B_{Si}^0$  defect would be an excited state. We identify two possible mechanisms for hole capture: (1) A two step mechanism involving hole capture in the onsite negative state, followed by reconfiguration to the neutral ground state,  $B_{Si}^-(on) + h^+ \rightarrow B_{Si}^0(on) \rightarrow B_{Si}^0(off)$ ; (2) Direct hole capture involving a strong electron phonon coupling,  $B_{Si}^-(on) + h^+ \rightarrow B_{Si}^0(off)$ . Here, ‘on/off’ stand for on/offsite configurations.

From Fig. 3(a) the barrier for the second step of mechanism (1) is estimated as  $\lesssim 0.1$  eV. As for mechanism (2), the capture of the hole by negatively charged  $B_{Si}^-(h)$  must involve a concomitant local deformation of the B-C bonds, so that the *moving* level shown in Fig. 3(b), which in this case is occupied, will emerge into the gap. A simple estimate of that barrier was found by calculating the potential energy of the defect for structures in the vicinity of offsite and onsite ground states of neutral and negatively charged  $B_{Si}(h)$ . These correspond to atomic coordinates  $\mathbf{R}^0$  and  $\mathbf{R}^-$ , respectively. Again, we define a one-dimensional coordinate  $R$ , such that all nuclear coordinates are constrained along an effective coupling direction of motion  $\mathbf{R} = \mathbf{R}^0(1 - R) + \mathbf{R}^- R$  (see for instance Refs. [80, 81] for further details).

Figure 4 shows the potential energy surface along the linear path joining ground state structures of  $B_{Si}^0(h)$  (with  $R = 0$ ) and  $B_{Si}^-(h)$  (with  $R = 1$ ). The energy of the two minima are separated in the energy scale by the calculated depth of the hole trap,  $E(-/0) - E_v = 0.32$  eV. A parabolic fit to the potential data in the vicinity of the two minima allows us to estimate the hole capture barrier for  $B_{Si}^-(h) + h^+ \rightarrow B_{Si}^0(h)$  as about  $E_\sigma \sim 0.1$  eV. Two additional features in Fig. 4 are highlighted — (i) the two parabola are not nested, suggesting that the capture mechanism involves a strong electron-phonon coupling, typical of deep centers [77]; (ii) the effective mode frequency of the neutral state (proportional to the curvature of the lower parabola) is substantially softer than that of the negative state. This is consistent with the formation of a B-C bond upon hole emission (or electron capture) by  $B_{Si}^0$ .

It is clear that the EPR data, in particular the  $^{13}C$  hyperfine splitting for this center [26, 29], cannot be accounted for by an EMT like onsite  $B_{Si}$  acceptor. On the contrary, the bistable model described above, proposes that  $B_{Si}$  is a deep hole trap, offering a physical explanation for the observations.